EVALUATION AND MODELING OF POWER SYSTEM COMPONENTS

by

ZACHARY RYAN BAILEY

A DISSERTATION

IN

ELECTRICAL ENGINEERING

Submitted to the Graduate Faculty
of The University of Texas at Arlington in
Partial Fulfillment of
the Requirements for
the Degree of

DOCTOR OF PHILOSOPHY

Approved

_____
Chairperson of the Committee

_____

_____

Accepted

_____
Dean of the Graduate School

May, 2022

ACKNOWLEDGEMENTS

I would like to thank my committee chair Dr. David Wetz for his guidance, mentorship, encouragement, and friendship throughout this process as a graduate student in Electrical Engineering here at the University of Texas at Arlington. His efforts, along with those of my committee members Drs. Wei-Jen Lee and Rasool Kenarangui, have encouraged me to pursue this field and continue my passion of studying power systems from an electrical perspective. I also appreciate the encouragement and support I received from Dr. Lynn Peterson during my time at UTA as I continued my passion of outreach within the nuclear community through the American Nuclear Society. In addition to the strong support from faculty, I also thank my fellow researchers in the Pulsed Power and Energy Lab who have been beside me through this time and have helped me to succeed in this field. I especially thank Alexander Johnston, Hayden Atchison, Cole Tschritter, Bradley Hannum, and Tyler Scoggin who have answered many questions and have helped with testing, data analysis, and peer review during my time in the lab. Lastly, none of this would have been possible without the support of my family and the encouragement I received from them.

I would like to thank ONR for their financial support of this effort through grants N00014-19-1-2031, N00174-20-1-0025, N00014-18-1-2714, N00014-18-1-2206, and N00014-17-1-2801. Any opinions and findings are those of the authors and not those of ONR.

TABLE OF CONTENTS

ABSTRACT

Future power system architectures will rely on a combination of rotating machines, power electronic devices, and energy storage. While it is possible to procure each component separately and conduct studies incorporating these devices into a system, increases in computing power and advanced computer modeling software have expanded the opportunity for research to be conducted on power system architectures without the need for actual hardware. This provides flexibility by allowing the user to design models of individual components that can then be integrated together or effortlessly interchanged depending on the function or testbed design that is being studied.

The UTA IDEAL testbed consists of multiple components that are representative of hardware found in many power system applications and this effort develops a process for modeling and characterization of three pieces of equipment. Though it is less power dense than many other chemistries, lithium-titanate-oxide (LTO) chemistry is one that is able to be symmetrically charged and discharged making it attractive in many applications. For this reason, two LTO cells were studied by first characterizing their properties and then capturing that characterization in a mathematical model that could potentially be used with current hardware in the testbed to simulate the presence of this battery without the requirement to purchase a large number of individual cells and supporting equipment. This is an important component within future power systems since energy storage devices can buffer renewable and non-stiff electrical power generation sources. This buffering capability was later shown during the modeling effort of the two motor-generator (M-G) sets within the testbed. Next, a method was developed for modeling a three-phase generator as well as a nine-phase generator connected to a bus containing a 1 kV lithium-ion battery.

During testing of the multi-phase generator, the buffering ability of the energy storage device was also demonstrated. Models were developed in MATLAB/Simulink® and the results from these models were comparted to the results obtained from actual hardware to show that the models accurately predict the hardware's behavior for specific cases with predefined output variable requirements.

LIST OF TABLES

LIST OF FIGURES

CHAPTER 1

INTRODUCTION

The first occurrence of electrification within seafaring vessels dates to 1903 in the *Vandal* with the introduction of diesel electric propulsion, but it wasn't until the 1920s that the first generation of electric ships utilizing electric propulsion drives were manufactured. These ships had steam turbine generators that powered the propeller motors and varied the propeller motor speed by varying the generator speed [1]; however, they soon began to disappear as diesel engines became predominant within the industry. It wasn't until power electronic devices emerged in the 1980s that the resurgence of the all-electric ship concept resurfaced and then gained traction with the development of variable speed drives (VSDs) in the 1990s [2]. Over time, there have been several studies performed to evaluate shipboard and terrestrial applications of MVAC, MVDC, or combination MVAC/MVDC microgrids. Some examples include cruise vessels, icebreakers, and liquefied natural gas (LNG) tankers that utilize electric propulsion and varying levels of AC and DC loads in either constant or pulsed power operation [3]. These case studies have shown that there are potential benefits but also drawbacks to incorporating these different microgrid structures.

Much of the discussion in favor or opposed to AC and/or DC power systems centers around either power quality, the size and availability of equipment and components, or personal preference. Since its inception, AC power, and MVAC microgrids by extension, have suffered from issues inherent to this power system arrangement including frequency matching and reactive power compensation. In an MVAC structure, prime movers must be synchronized, and the frequency of these machines must be adjusted to maintain the AC

frequency at its required rating (i.e., 60 Hz) regardless of loading conditions. This limits the ability to adjust and optimize the parameters of these machines as loads are stepped on and off and creates a less fuel efficient and more environmentally unfriendly solution. Introducing DC energy storage into an AC distribution system requires AC/DC and DC/AC converters. Rectified generators and machines do not require phase angle synchronization and the previously discussed frequency matching is eliminated leading to the possibility of connecting a diverse set of power sources, energy storage, and loads. These machines also benefit from a reduction in size due to the ability to operate at higher rotational speeds and lower torque while generating a higher power density. They have the capability of optimization where parameters can be calculated instantaneously based upon current loading characteristics and then subsequently adjusted to prevent a voltage unbalance at grid connections. Machines designed for MVDC grids are often poly-phase providing a higher quality of rectified DC power, improved reliability, and a lower current rating per phase as opposed to the traditional three phase machines incorporated into many MVAC systems [4].

Depending upon the voltage amplitude, DC power distribution systems provide a slightly easier opportunity for the inclusion of energy storage since it can be floated on the bus if the battery voltage and distribution voltage are well matched. In MVDC systems, the distribution voltage is almost certainly much higher than the energy storage voltage and therefore DC/DC converters are required. Converters stepping up or down DC voltages to MVDC levels are rare and hard to find commercially. Studies have been performed considering the inclusion of many different forms of energy storage including batteries, capacitors, flywheels, and hybrid combinations of these technologies. Ragone charts, like

the one seen in Figure 1, compare the energy density and power density of the many technologies and highlight their wide-ranging capabilities. Li-ion batteries offer a high combined power and energy density making them very attractive, but they have lifetime and safety concerns that have tempered their use. Supercapacitors offer a high-power density but modest energy density. Batteries and ultracapacitors can serve as both a source or load for the purpose of buffering power quality of connected generators during transient loading operations and this makes them very attractive. High-speed flywheels offer a high combined power and energy density, but they are expensive and, in some cases, difficult to manufacture. Hybrid energy storage systems (ESSs) that employ multiple technologies, in a controlled manner, afford the benefits of each to be realized and they have been evaluated in recent years with great success [5, 6].

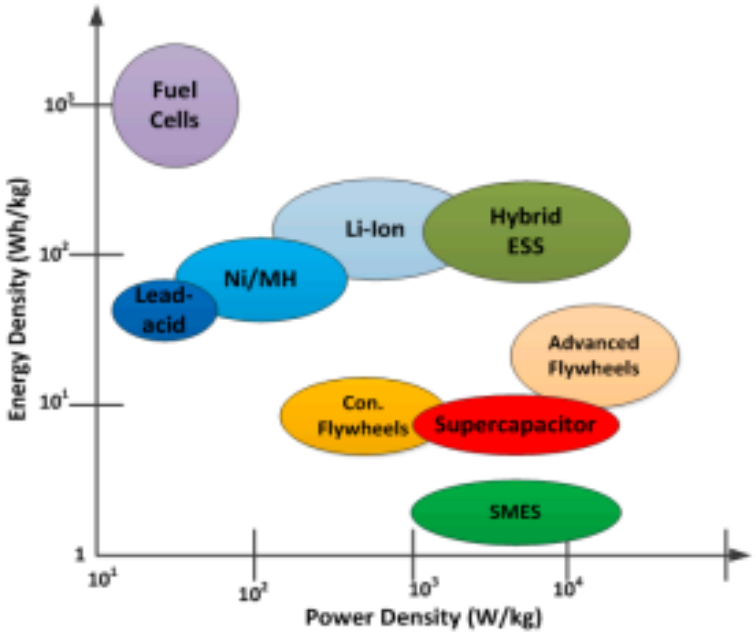

Figure 1. Ragone chart comparing the power and energy density of various energy storage technologies [7]

CHAPTER 2

BACKGROUND

It has been proposed by many that next generation Navy ships employ a zonal power system architecture that uses either MVDC and/or MVAC power distribution [8-10]. As an illustration of what this would look like, a zonal MVDC architecture proposed by Doerry is shown in Figure 2. Because MVDC distribution networks are two wire systems that carry lower current, they are attractive, but they look very similar to MVAC architectures at the granularity shown in Figure 2. Each zone is connected to the main distribution using a longitudinal MVAC or MVDC bus with a distribution node at each zone. A zonal architecture, when coupled with intelligent sensing and controls, enables the power system to remain resilient and flexible when it comes to uniquely optimizing performance in various operational scenarios. Within each zone, it is proposed that there be propulsion motors, auxiliary turbine generator (ATGs) sets, power distribution equipment, critical and non-critical mission loads (MLs), power conditioning modules (PCMs), and either point and/or distributed energy storage systems. One advantage of the zonal architecture is the ability to design each zone to limit the propagation of damage between adjacent zones and improve overall reliability within the ship. When a zone needs energy from a neighboring zone with excess generation capacity, the MVAC and/or MVDC distribution bus can be used to share available power across zones. PCMs capable of operating at MVAC and/or MVDC are required, and this is a significant challenge.

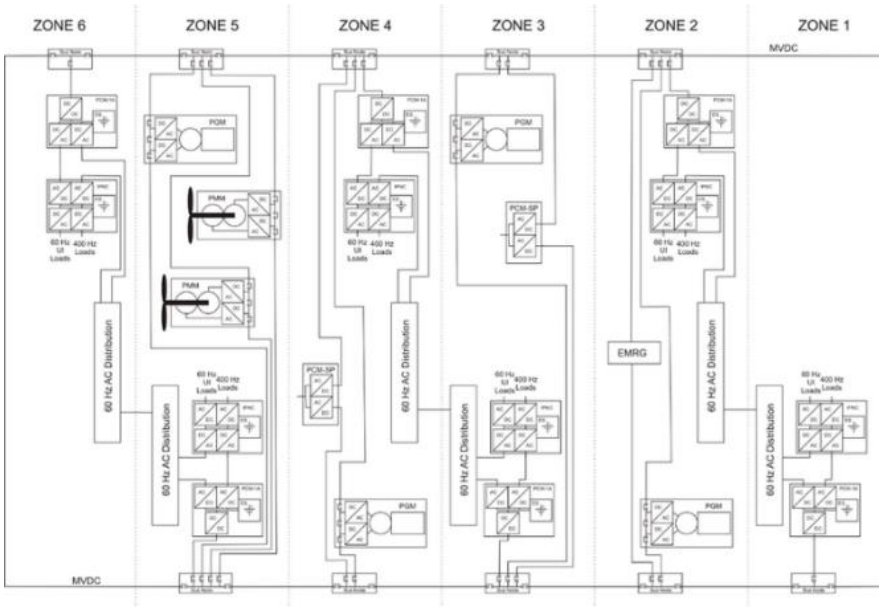

Figure 2. Simplified zonal MVDC architecture design [8].

The design and compartmentalization of each zone's components is determined by addressing specific design threat outcomes that ensure that the ship will perform within an acceptable range during each of the possible expected and unexpected operational conditions [9]. Although zonal architectures can consist of any number of zones, the size of each one should be limited to approximately 15% of the length of the ship to limit the amount of safety significant or mission critical equipment within any single zone [10]. Although ships may be designed with a single bus, the redundancy provided by two longitudinal buses, running forward to aft on the starboard and port side of the ship, provides greater survivability and quality of service in the event one bus is removed from service due to a fault or damage [8-10]. Together, the components within an MVDC architecture comprise an integrated power system (IPS) where service loads and pulsed loads are all sourced from the same electrical power source.

The design of each zone varies based on the location of equipment within the ship and the individual function the equipment is designed to perform. Monitoring and control of each zone and all the components in it is critical and is something that is being studied [11]. During operation, a dedicated controller monitors the state of health (SoH) and state of charge (SoC) of the energy storage and decisions can be made based on the current and forecasted load requirements. The controller can control the sourcing and sinking of the energy storage power to limit excessive harmonic fluctuations observed by the ATGs, mitigate load shedding requirements, and provide ride through if generators drop offline. The battery sinks energy when the generator is underloaded and sources energy when the generator is overloaded reducing the power requirement seen by the generator and simultaneously reducing the mechanical stress which can lead to increased generator maintenance or failure [8].

On paper, and theoretically, a zonal architecture employing MVAC and MVDC power distribution holds significant promise. Electrical grids around the world rely on MVAC for transmission of power. Transformers are used to step up/down the voltage and power converters that are suited for operation at lower AC voltages are widely available and can be employed. Advances made in the development of high voltage power electronic switches, especially Silicon Carbide (SiC) has made multi-level AC/AC and DC/AC designs operating at 13.8 kVAC commercially available but there are not many suppliers making them. Though transformers are viable options for use in ships, they are heavy and introduce significant inductance into the power system. A zonal architecture requires many transformers, and it can start to become unattractive quickly but its at least possible. If MVAC voltages no higher than 13.8 kV are used for power distribution, the availability of

power electronic technologies makes this approach feasible but much more work is needed before it will be implemented.

As shown in Table 1, IEEE has provided some distinction between what is possible in current MVDC power distribution systems and what is possible in the future [12]. It can be inferred from this table that components are available to field MVDC designs operating at less than 5 kVDC but not higher. Though many are talking about MVDC power distribution systems higher than 5 kVDC, there is currently a lack of market driven demand and this makes it difficult. Industry leaders such as GE, Siemens, and ABB, among others, have begun to develop commercial products aimed at filling this gap which are currently being marketed to the wind, solar, and other terrestrial microgrid applications but they are limited.

Table 1. IEEE Recommendations for Voltage Classifications of MVDC Power Systems [13]

	Nominal MVDC Voltage [kV]	Maximum MVDC Voltage [kV]
Established MVDC Designs	1.5 (± 0.75)	2 (± 1)
	3 (± 1.5)	5 (± 2.5)
Future MVDC Designs	6 (± 3)	10 (± 5)
	12 (± 6)	16 (± 8)
	18 (± 9)	22 (± 11)
	24 (± 12)	28 (± 14)
	30 (± 15)	34 (± 17)

2.1 MVDC Architecture

The concept of a DC grid structure originated with Thomas Edison but was criticized at the time for its inability to easily transform the voltage from one level to another. This was not an issue with AC power where transformers can be integrated to step-up or step-

down the voltage as necessary. As power electronic devices have evolved, Edison's idea of a DC power distribution grid has once again become a possibility. Figure 3 shows a concept of what a MVDC smart grid might look like. It has multiple sources and loads connected to a single MVDC. Power electronic converters are used to convert voltage as needed. There are presently examples of MVDC microgrids in electrical rails for trains, space applications, data centers, and telecommunications.

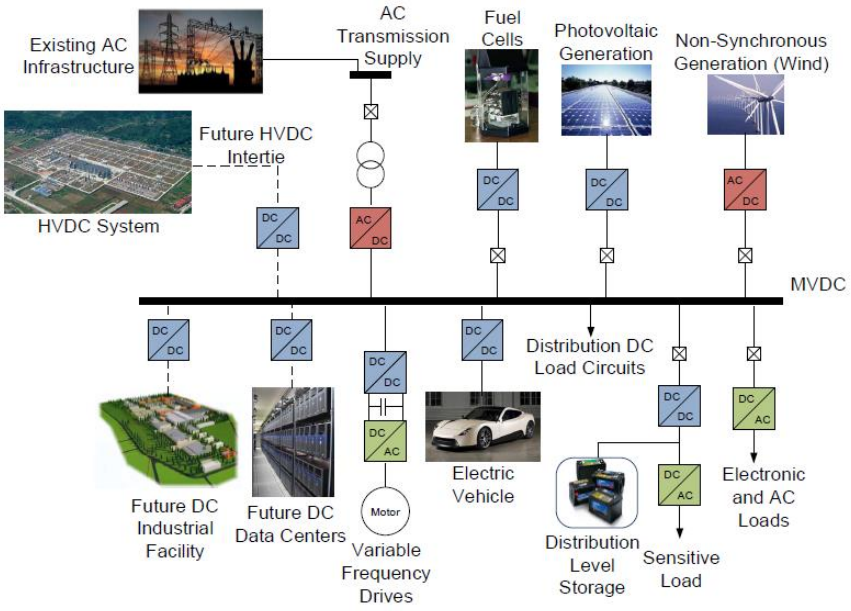

Figure 3. A simplified MVDC microgrid structure [14].

Since MVDC systems only require two wires, carry low current, and don't utilize heavy transformers, it is attractive to the shipping industry. If the bus voltage is low, <1 kVDC, it is easier to integrate energy storage but as the voltage increases, it becomes equally challenging since DC/DC converters are limited at voltages higher than 6 kVDC.

2.2 UTA's Integrated Distributed Energy Analysis Laboratory (IDEAL) Testbed

The UTA IDEAL testbed was constructed to emulate a single zone of an MVAC/MVDC electric ship. The testbed includes an electric motor/generator set, multiple AC and DC buses, power converters, transformers, variable resistive loads, and a lithium iron phosphate (LFP) battery. Figure 4 presents an electrical one-line diagram of the testbed and Figure 5 presents a graphical one-line diagram. Figure 4 highlights the capability along with placement of the current and voltage monitoring distributed throughout. A brief description of the hardware is provided, and it has been previously discussed at length in [15-16]. The primary source of AC power for the testbed is a Motor-Generator (M-G) set controlled by a Variable Frequency Drive (VFD) that supplies 480 VAC and has a maximum power rating of 150 kW. It is a four-pole synchronous generator with rotational frequency of 1500 – 2000 rpm controlled using a four-pole 300 hp induction motor. The generator's output voltage can be altered by +/- 20% and its frequency can be altered between 50 to 67 Hz. Frequency control is implemented using two independent 0 – 10 V analog reference signals supplied by an external control source. With this capability, alternative generation sources are emulated through model execution on a real-time simulator.

The M-G set supplies three branches. Two branches are connected to AC/DC converters and one is connected to an AC/AC converter. The interconnection of these four devices forms a point of common coupling (PCC). In Figure 4, the top branch runs from the PCC to a 225 kW GE MV6000 five-level power electronic drive AC/AC converter. Within the MV6000, a step-up eighteen-phase transformer and thirty-six-pulse diode rectifier creates a 6 kV DC link and a five – level IGBT inverter inverts the DC link to

generate a three phase 4160 VAC output voltage. Using 0 – 10 V analog reference signals, the output voltage and frequency of the MV6000 can be adjusted between 0.8 p.u – 1.1 p.u. and 50 Hz – 70 Hz, respectively. The MV6000's 4160 VAC output bus is split into two branches, one to a transformer and one into an AC/DC converter. The transformer is a 4160/480 VAC step-down transformer that feeds directly into a 350 kW, 480 VAC resistive load from Mosebach Inc. The load has a 1 kW step resolution controlled either directly on its own control panel or through digital signals supplied by the testbed's control system and emulates traditional shipboard hotel loads (i.e., lighting, heaters, etc.), which typically remain quasi-static once stepped on. The second branch of the 4160 VAC PCC feeds into an AC/DC rectifier (GE) comprised of an eighteen-phase transformer and thirty-six pulse diode rectifier. This is the same rectifier within the MV6000 creating a 6 kVDC bus voltage loaded by a resistive Mosebach Inc load bank. This bus is loaded with a constant load emulating a non-variable baseload.

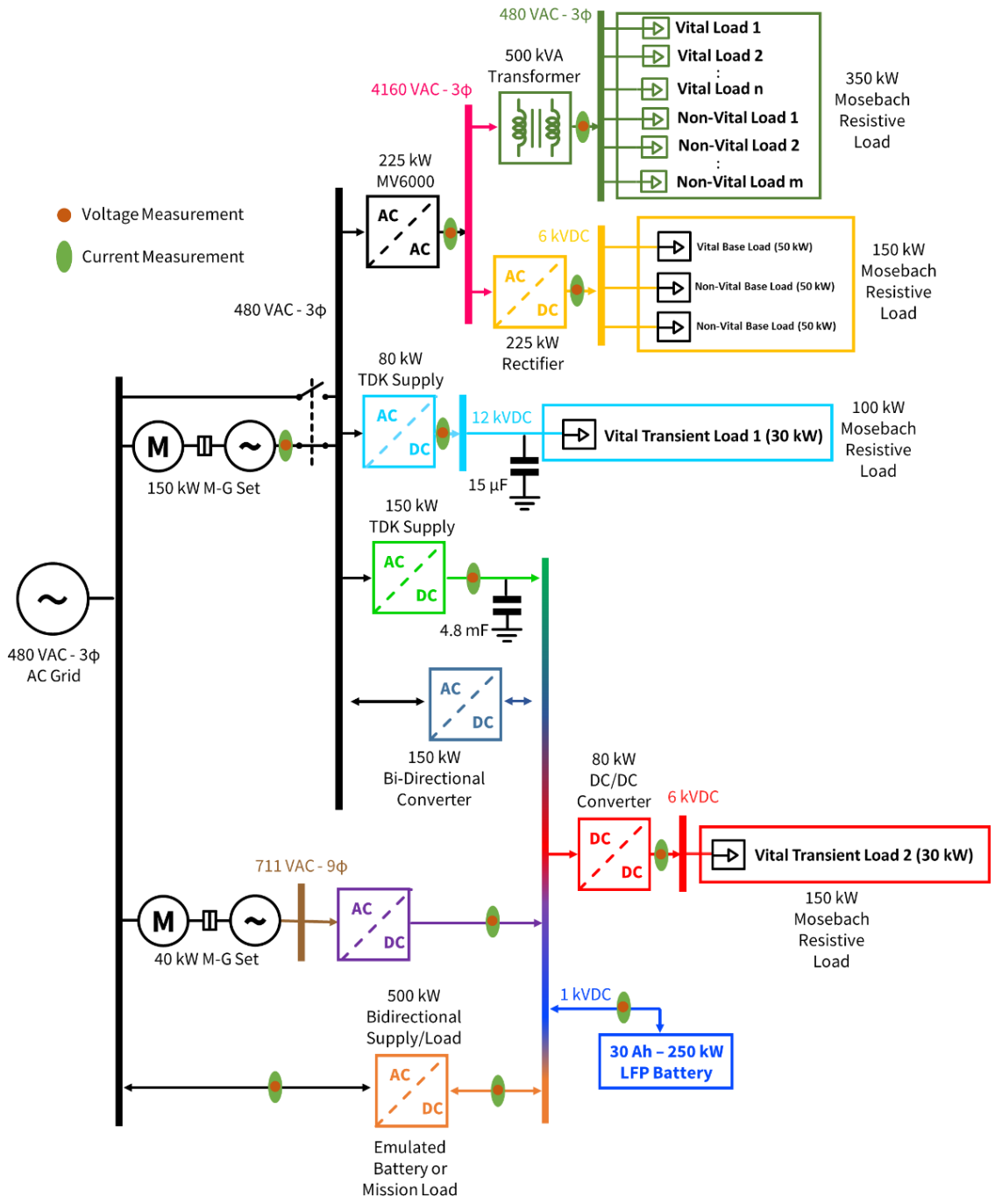

Figure 4. UTA IDEAL testbed one-line diagram.

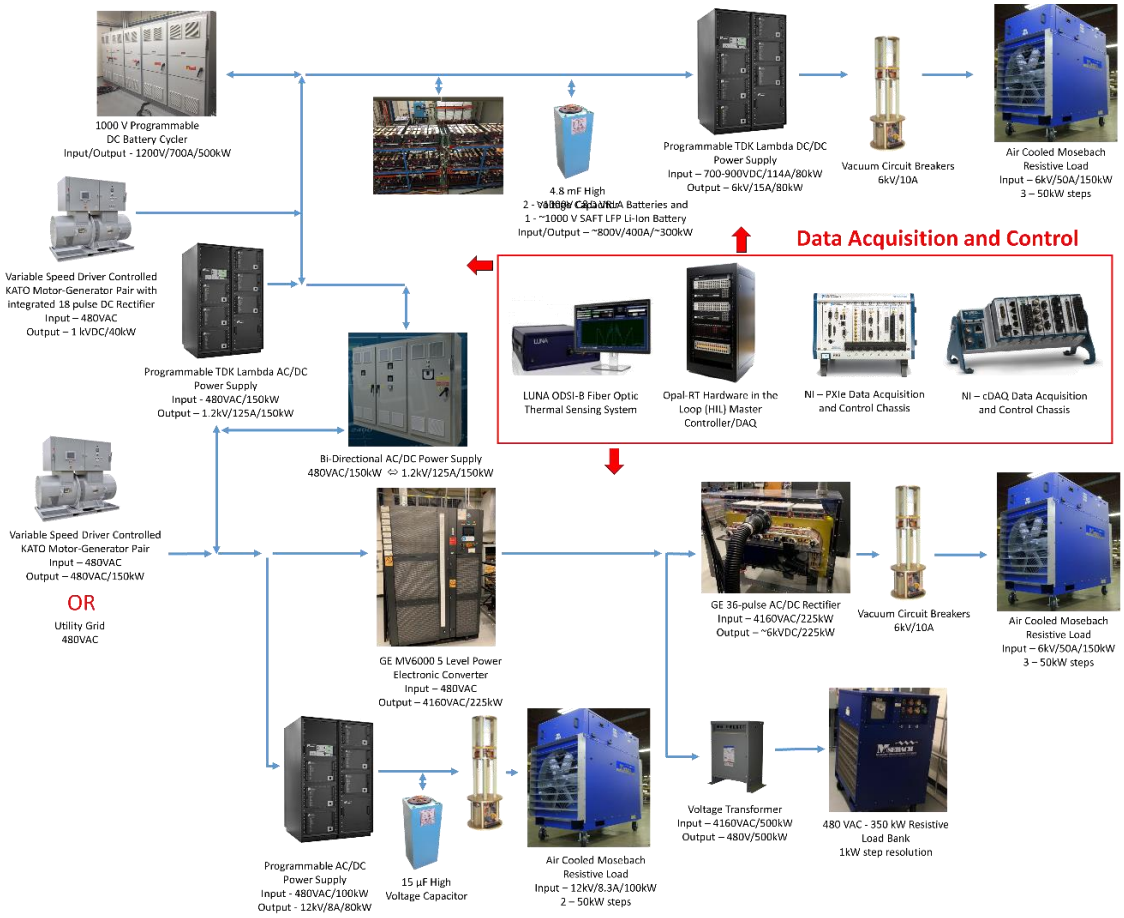

Figure 5. Pictorial one-line diagram of the IDEAL MV DC/AC distributed generation source testbed as it is assembled in the UT Arlington Pulsed Power and Energy Laboratory.

The middle electrical branch from the 480 VAC PCC consists of an 80 kW AC/DC converter that takes 480 VAC and steps it up to 12 kVDC. This converter is comprised of two capacitive charging power supplies that work in a host-client mode. These capacitor chargers must always be loaded when on, so a 15 µF capacitor is floated on the bus for safety. The converter is operated in a current-controlled mode and loaded using a Mosebach resistive load bank rated as high as 100 kW at 12 kVDC. The current limit of the power supply is controlled using 0 – 10 V analog reference signals supplied by the host

controller. Since it is fed into a resistive load, the voltage of the output bus varies as a function of the current. This supply and load are used to emulate a high power transient electrical load through modulation of the output current.

In the lower electrical branch of Figure 4, the 480 VAC PCC supplies an AC/DC power electronic converter feeding a ~1 kVDC PCC. The supply is rated up to 1.2 kVDC and 150 kW with a 4.8 mF capacitor floated on the output bus to protect the supply. The upper branch of the 1 kVDC PCC breaks out to a DC/DC converter that takes the 1 kVDC bus and steps it up to 6 kVDC. This converter is rated at 80 kW loaded using a second 6 kVDC Mosebach resistive load identical to the one installed at the output of the AC/DC rectifier discussed previously. The output current is modulated the same way as the 12 kVDC converter used to emulate a second high power transient load. This branch is also supplied by an M-G set that produces 711 VAC with active rectification to 1 kVDC and has a maximum power rating of 40 kW. It is a 120 Hz, nine phase synchronous generator with an output voltage and frequency that can be altered by +/- 20% using 0 – 10 VAC inputs or the control panel of the front of the machine. On the lower branch of the 1 kVDC PCC, the LFP battery floats on the bus acting as a buffer. Excess power from the generator is used to charge the battery enabling the system to maintain a base generator load. When power draw exceeds intended base load, the battery supplies the deficiency to the transient 6 kVDC load. The power supplied by the AC/DC converter and the battery is achieved by setting the AC/DC converter's voltage higher than the intended bus voltage and imposing a current limit. Current and voltage setpoints are controlled using analog reference signals supplied by the host controller. If the battery is not at 100% or 0% SOC, this power shuffle is possible. All the set points mentioned here are directly controlled using optimization

principles and control parameters set by the user in an NI controller. The bi-directional converter between the 480 VAC bus and the 1 kVDC bus was only recently added and once commissioned it will provide enable the battery to be able to buffer any load in the bus instead of only the one 6 kVDC load that it can now.

Comprehensive voltage and current measurements are made as indicated in Figure 4. All current measurements are made using closed loop Hall Effect current sensors (Harting 100 A and 300 A sensors) chosen for their 50 kHz bandwidth and 0.5% accuracy. Voltage measurements use one of two types of differential voltage probes: a 1.4 kV, 25 MHz, differential voltage probe manufactured by Pico Technology (model TA057), and a 7.0 kV, 70 MHz, differential voltage probe also manufactured by Pico Technologies (model TA044). All voltage and current measurements are acquired using an NI PXIe chassis instrumented with data acquisition cards interconnected with the NI cDAQ controller. Network variables are used to pass real-time measurements back to the host system for control and decision-making.

In summary, the testbed integrates 480 VAC and 4160 VAC sources, a 1 kVDC bus sourced by a multi-phase generator, AC/DC converters and a Li-ion battery, a 6 kVDC bus supplied by both AC/DC and DC/DC converters, and a 12 kVDC bus sourced by an AC/DC converter. The testbed is being used to study intelligent control of the power electronic converters and the use of a battery to buffer rotating AC sources. This testbed was commissioned to demonstrate the viability of hybrid MVAC/MVDC grids and provides a method for studying architecture for use in future shipboard power systems.

2.4 Verification and Validation

The UTA IDEAL testbed was designed to incorporate a variety of engine-generator sets, power supplies, loads, and the support equipment required to produce and transmit energy. This provides a method of study that is specific to the equipment procured; however, future studies might utilize a variety of equipment and procuring each of these components separately to incorporate into a testbed for evaluation can become costly and be substantial in time and space. One solution that limits the amount of time and money allocated toward hardware is the use of software applications to emulate these components. However, in creating these computer models, it is necessary to show that they fulfill their stated function and adequately model the individual component and larger power system in which the component resides.

During development of these emulated components, a process of verification and validation (V&V) must be performed to ensure that the software or computer models accurately capture the necessary details within the domain in which the model is being developed. Initial verbiage describing this process was published by Schlesinger et al in 1979 [17] and has been adapted to processes involving computational modeling by standards such as IEEE-STD-610 [18]. In the context of hardware emulation, verification is an iterative process that requires a developer to routinely check that the model being developed continues to fall within the specifications set forth before the modeling effort began, and then validation is performed to show that the model does meet these required expectations. This is graphically illustrated in Figure 6 with the left side representing the verification process and the right side representing the validation process. By following this process, most of the problem identification and resolution occurs during the

verification process where multiple models might be created before a valid model is chosen, but often the most parsimonious model with the highest fidelity becomes the fully verified and validated model for a given application [19].

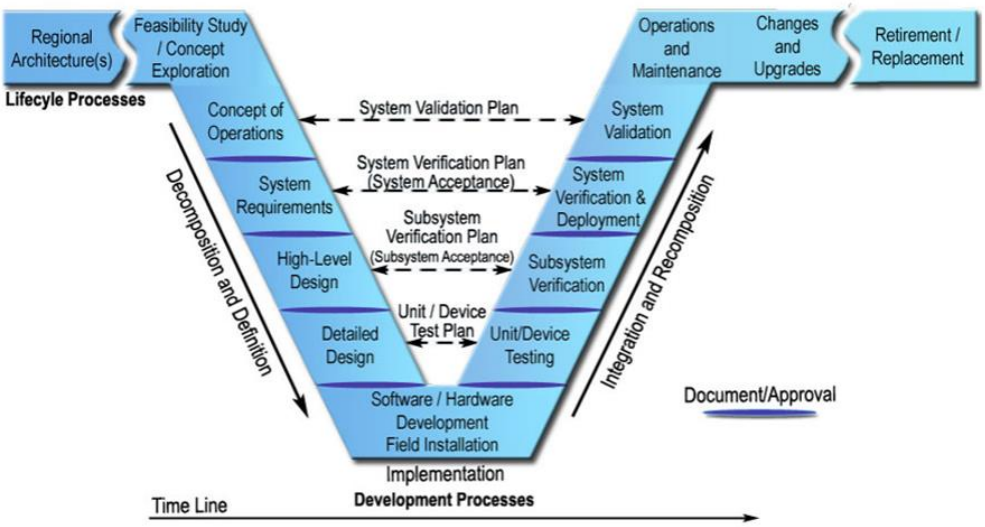

Figure 6. Pictorial description of the Verification and Validation process [22].

As previously mentioned, model V&V is performed over a predetermined domain or application because it is normally not feasible to fully verify and validate a model over a complete gamut of applicability. Therefore, determining that a model is valid requires that the accuracy of its output variables are within an acceptable range for each question, scenario, or purpose that the model is being designed to answer and these acceptable ranges must be determined and set prior to the commencement of the modeling effort [19-21]. This validation can then be performed by comparing simulation data with empirical results obtained from actual hardware using testing scenarios designed according to the requirements of the model [20].

Three components particular to the testbed were studied using this V&V methodology: the battery, the 480 VAC three-phase M-G set, and the 769 VAC/1 kVDC nine-phase M-G set. Both M-G sets are hardware that have been procured and installed within the testbed architecture; however, the battery studied here is a separate Li-ion chemistry that has not been procured at the 1 kVDC level. Battery studies were conducted at the cell level and then extrapolated to higher voltages using software developed from the tests performed. The process of developing test plans, conducting experimental studies, and subsequent model development is documented in this research.

CHAPTER 3

LITHIUM-ION BATTERY STUDY

Future power system architectures will rely on energy storage to buffer renewable and non-stiff electrical power generation sources. Specifically, a battery would be capable of sinking energy when the generator is underloaded and sourcing energy when the generator is overloaded reducing the power requirement seen by the generator and simultaneously reducing the mechanical stress which can lead to increased generator maintenance or failure [8]. This operation of sourcing and sinking power limits excessive harmonic fluctuations observed by the generator during transient loading events which can occur as either a single high-power load or an amalgamation of smaller loads initiated simultaneously. Lithium-ion batteries have long been considered a front runner in applications such as these where both power and energy density are needed to meet the always fluctuating source and load demand. These batteries have already developed a proven track record in consumer electronics, but certain lithium-ion chemistries have also shown great promise in the area of energy storage applications [23]. Though it is less power dense than many other chemistries, lithium-titanate-oxide ($Li_4Ti_5O_{12}$), or LTO, chemistry provides a safer alternative with symmetric charging and discharging and exceptional lifetime. This makes LTO batteries advantageous for high peak-power or pulse-power applications. These characteristics, and others, are compared between multiple lithium-ion chemistries in the spider chart in Figure 7.

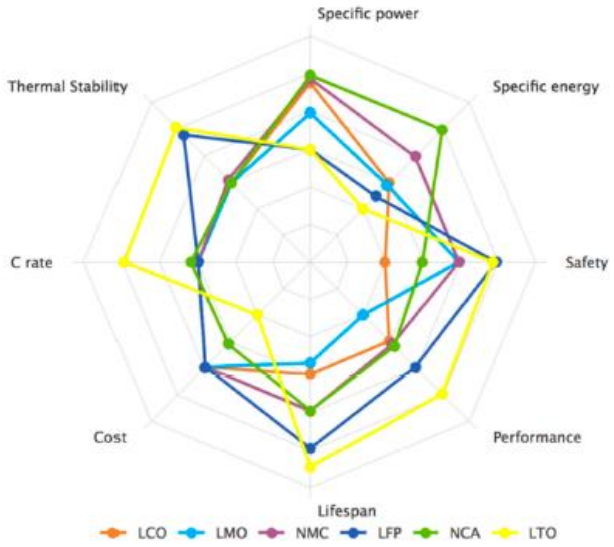

Figure 7. Spider chart comparing various lithium-ion chemistries in functional areas of performance [24].

All lithium-ion batteries employ a cathode that releases lithium ions to the anode during a charging process and an anode that supplies the cathode with lithium ions during the discharging process [25-26]. The difference between these technologies is dependent on the construction material of the cathode and anode. While many lithium-ion batteries use carbon or carbon-based anodes, LTO cells use the metal oxide lithium-titanate as the lattice for the anode material [27-29]. This material creates a charge reaction given by the following equation:

$$Li_{4/3}Ti_{5/3}O_4 + Li^+ + e^- \rightarrow Li_{7/3}Ti_{5/3}O_4 \quad (1)$$

The discharge reaction then becomes the reverse reaction of Equation (1) [27]. The charging and discharging process have been shown to produce negligible mechanical stress

on the lattice structure of the LTO, which contributes to the longer lifetime of this particular chemistry [30]. This stability leads to less capacity fade after repeated lifetime cycling, and studies have shown that LTO cells can have a lifetime of 15-20 years depending on cycling rate [31-32]. Also, LTO cells have been shown to suffer less deleterious effects when stored in higher temperature enclosures and subjected to quick charging cycles; whereas, lithium batteries that employ a graphite anode often experience higher rates of capacity fade when exposed to these forms of stress [33]. The combination of these properties make LTO technology especially favorable for long-life applications such as vehicles and military applications [31].

Although there are many advantages to LTO technology, one disadvantage is the lower cell voltage often reported for these cells. The cell voltage of an LTO cell is roughly two thirds that of a conventional lithium-ion battery. While this does have the effect of decreasing the specific energy of that cell it conversely has the advantage of reducing the amount of lithium deposition that occurs which also contributes to the longer cycle life of these cells [25].

3.1 Cell Summary

One of the primary manufacturers of LTO cells is Toshiba and recently they developed individual 10 Ah, 20 Ah, and 23 Ah capacity cells. A summary of each of these LTO cells is shown in Figure 7 as a Ragone chart. According to the Ragone chart, while the 20 Ah and 23 Ah cells have comparable power density, they have a larger energy density than the 10 Ah cell while the 10 Ah cell offers a higher power density than both of the 20 and 23 Ah cells. All three Toshiba cells are designed with the same form factor of

W116 x D22 x H106 mm which gives these cells a prismatic shape. The terminals extend as tabs on each side of the top of the cell, and there is a separate contact dedicated for voltage sensing. Figure 9 shows a procured sample of a Toshiba cell.

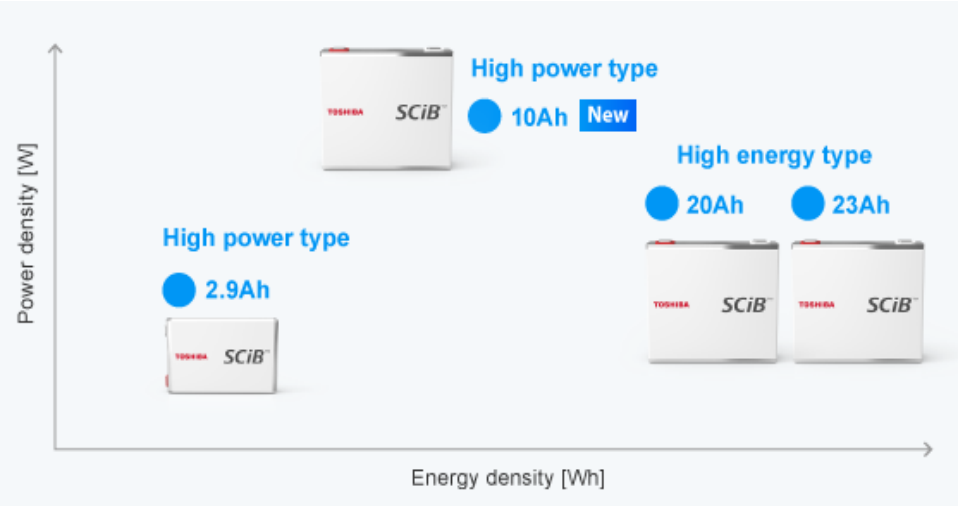

Figure 8. Ragone chart comparison of the Toshiba 10 Ah, 20 Ah, and 23 Ah SCiB LTO cells.

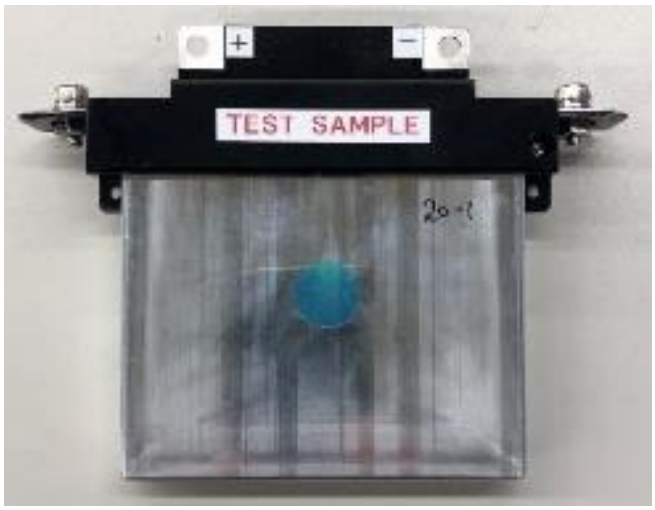

Figure 9. Toshiba prismatic LTO cell.

Table 2 shows the properties of each of the three Toshiba cells previously described. As can be seen from this table and the above Ragone chart in Figure 8, the 20 Ah and 23 Ah cells are similar except for capacity. Therefore, this study consists of characterizing the differences between the energy dense 23 Ah cell and the power dense 10 Ah cell.

Table 2. Operational conditions for each LTO cell

Parameter	**10 Ah Cell**	**20 Ah Cell**	**23 Ah Cell**
Minimum Voltage	1.8 V	1.5 V	1.5 V
Maximum Voltage	2.8 V	2.7 V	2.7 V
Maximum Continuous Discharge Current	110 A (11C)	100 A (5C)	100 A (4.3C)
Maximum Continuous Charge Current	110 A (11C)	100 A (5C)	100 A (4.3C)
Operating Temperature	-20°C to 55°C	-30°C to 55°C	-30°C to 55°C

3.2 LTO Experimental Test Plan

The work performed in this study is aimed at electrically and thermally characterizing the LTO cells' properties and capabilities. The cells in this study were tested using four separate experiments, each of which will be described later and are listed as follows:

1. C rate characterization
2. Impedance measurement
3. Continuous duty cycle characterization
4. Capacity fade measurement through repeated cycling.

3.2.1 C Rate Characterization

Before being subjected to lifetime cycle testing, each cell was put through a characterization study involving various charge and discharge rates. This has been done to get an understanding of initial differences in the cells' performance during different

charge/discharge cycles. Based on this characterization, the equivalent series resistance (ESR) for each cell can be calculated as a function of depth of discharge (% DoD). Additionally, the discharge curves can be used to determine the conduction voltage for each cell, the usable capacity, and the thermal rise that occurs during each charge/discharge cycle at varying rates of interest.

After completion of 2500 cycles in the life cycle experiments, listed as Experiment 4 above that will be discussed soon, the cells were re-characterized using the same charge/discharge rates to determine the percent change in capacity that has occurred due to lifetime cycling. These discharge curves are once again used to calculate the ESR as a function of DoD to determine if there is a measurable change in internal resistance due to aging.

3.2.2 Impedance Measurement

Each cells' impedance was characterized using electrochemical impedance spectroscopy (EIS). EIS is a perturbative characterization, allowing the real and imaginary components of a cell's impedance to be measured as a function of frequency. EIS can be performed using two different methods: galvanostatic or potentiostatic. Galvanostatic mode perturbs the cell with a precise AC current and sweeps through a pre-defined frequency range. At each frequency step, the perturbation voltage and current are measured to determine the cell's real and imaginary impedance values. The same concept is used in potentiostatic mode but instead of perturbing the cell with a set current, the cell is perturbed at a set voltage. This concept is illustrated in Figure 10, where the input signal, voltage, is applied to an electrochemical system and the output signal, current, is measured along with

the phase shift between it and the input signal. This phase shift can then be correlated to different electrical characteristics of the cell for development of an electrochemical circuit.

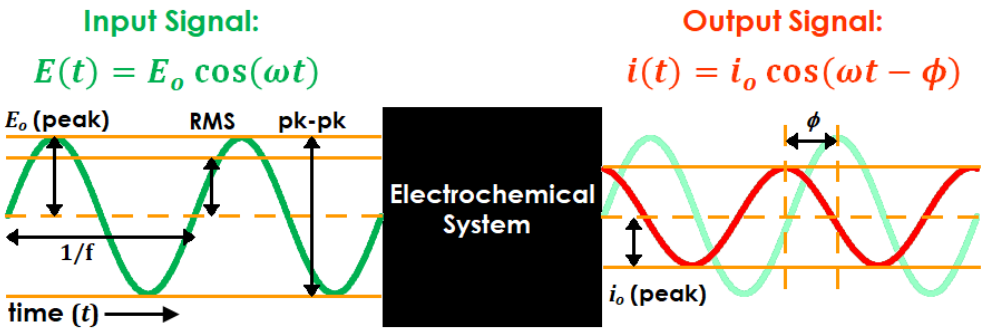

Figure 10. Concept employed in EIS testing of an electrochemical cell [34].

In these experiments, an Autolab PGSTAT302N is used along with a 20 A booster, seen in Figure 11. Multiple cells from each manufacturer are characterized using EIS in the *galvanostatic* mode at 2.5 A from 1 kHz to 10 mHz. The cell's impedance is measured across its respectable usable voltage range from 100% to 20%, in 10% increments.

Key features	
Electrode connections	2, 3 and 4
Potential range	+/- 10 V
Compliance voltage	+/- 30 V
Maximum current	+/- 2 A (20 A with BOOSTER20A)
Current ranges	1 A to 10 nA (100 pA with ECD module)
Potential accuracy	+/- 0.2 %
Potential resolution	0.3 µV
Current accuracy	+/- 0.2 %
Current resolution	0.0003 % (of current range)
Input impedance	> 1 TOhm
Potentiostat bandwidth	1 MHz
Computer interface	USB
Control software	NOVA

Figure 11. The Autolab PGSTAT302N used in this experiment, along with some of its key features [35].

After the cells have been characterized using EIS, they next undergo single pulsed discharges into a near matched impedance load. This is accomplished using a custom experimental testbed, seen in Figure 12. The testbed was designed to handle 10 kA peak current pulsed discharges from electrochemical energy storage devices and can achieve load impedances as low as ~350 μΩ. The testbed was used in these experiments to study each cell's peak power density by discharging the device under test for 200 ms into the low impedance load. In this round of experimentation, each cell was experimentally pulsed using the test stand three times. Between each pulse, the cell under test is removed from the stand, recharged, and then replaced in the stand and tested again. This provides a degree of statistical variation into the tests to ensure that the results are statistically relevant.

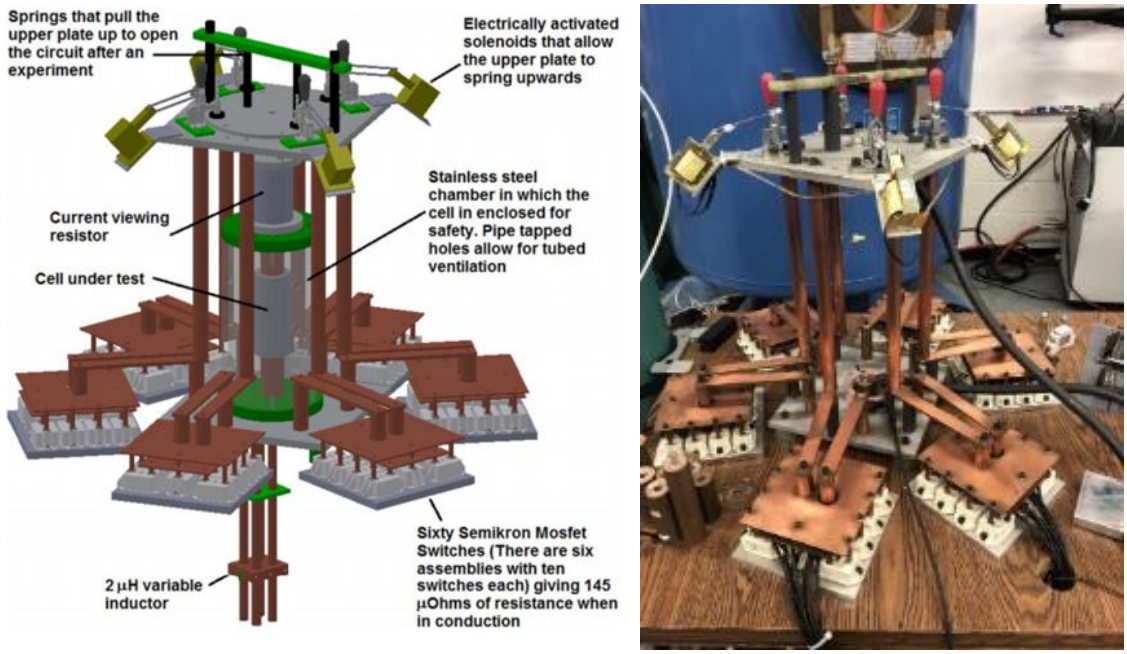

Figure 12. CAD drawing of the custom experimental testbed (left) along with a photograph of the testbed (right).

3.2.3 Continuous Duty Cycle Characterization

Each cell undergoes a series of repetitive pulsed cycling to evaluate its electrical and thermal characteristics. Repetitive pulsing is performed at as many as five different rates (depending on the maximum recommended current by the manufacturer) until thermal equilibrium is reached. At each rate the cell is cycled at 100% duty cycle, with 50% consisting of a charge and 50% consisting of a discharge. This means that there is ideally a 0 J net energy change in the cell after each charge/discharge cycle. Each cycle operates the cell approximately between 90% and 40% of its rated voltage. Each test is conducted with the cell placed inside a temperature chamber that is held at 20°C and then again at 40°C. Each cell is instrumented with a T-type thermocouple placed at the center of the cell to monitor its body temperature during testing. The repetitive pulsed cycling is performed using a Chroma model 63209 programmable load, with the capability of sinking current as high as 1000 A and a Sorensen power supply capable of sourcing up to 188 A shown in Figure 13. The load and supplies are controlled remotely using SCPI communication via GPIB and LXI, respectively. A custom virtual instrument (VI) was created using LabVIEW to control the supplies and loads, monitor the system for thermal or voltage cutoffs, and record the resulting voltage, current, and thermal data.

Figure 13. Photographs of the programmable load and supplies used to cycle the cells and modules for this experiment.

3.2.4 Capacity Fade Measurement through Repeated Cycling

One of the main purposes of this study is to determine the percent of original capacity that fades as a cell undergoes repeated cycling at high continuous rate. The pulse profiles are designed to have an ‘on time’, during which the Chroma 63209 programmable load is actively discharging the cell, and an ‘off time’, in which no charge or discharge is occurring. As an example, a pulse profile of 5 seconds on/5 seconds off commands the load to source power from the cell for five seconds followed by a 5 second rest. After the 5 second rest period, the profile is repeated. This continues until the cell either reaches a temperature cut-off or a minimum cell voltage. When the cell reaches a cut-off, this is considered one cycle. There are three pulse profiles utilized in this test: 5 seconds on/5 seconds off, 5 seconds on/1 second off, and 30 seconds on/5 seconds off. A T-type thermocouple is placed at the center of each cell to monitor the cell’s body temperature during testing. The load and supplies are controlled remotely using SCPI communication via GPIB and LXI, respectively. A custom virtual instrument (VI) was created using

LabVIEW to control the supplies and loads, monitor the system for thermal or voltage cutoffs, and record the resulting voltage, current, and thermal data.

3.3 Experimental Setups

Each of the experimental test series described above has its own unique experimental setup that will be described here.

3.3.1 C Rate Characterization

Each cell was initially characterized in open air using a Maccor cycler as shown in Figure 14. The characterization process consisted of cycling the cell through continuous charge/discharge cycles at various rates between the manufacturer's suggested rate through to the maximum rate allowed by the datasheet. Each cycle consists of a constant current/constant voltage charge with a C/10 cut-off followed by a symmetric discharge at the same rate. The capacity for each continuous discharge was determined by plotting the cell voltage versus capacity for each discharge rate. A thermocouple is also attached to the body of each cell during this characterization process to monitor temperature changes during charge/discharge cycles and record the maximum temperature acquired during each cycle.

Figure 14. A Maccor cycler used for cell characterization (left) and two Toshiba cells placed on an open-air cart for characterization (left).

Cell characterization, as described here, was performed initially for establishing a baseline and after lifetime cycling of the cells. The ESR calculation, described below in Equation (2), was also performed for both baseline and after 2500 cycles and plotted as a percent DoD. This showed a comparison between initial capacity and ESR and final capacity and ESR after 2500 cycles.

3.3.2 Impedance Measurement

The Toshiba cells are fabricated with tabs at each terminal along with a separate location designed specifically for voltage sense. These tabs are used for connecting the working and common electrode of the potentiostat to the cell for charge/discharge during EIS testing. Sense leads from the potentiostat are connected to the voltage sense tabs on the cells for monitoring the cell under tests' voltage. Figure 15 contains a photograph of a

Toshiba cell with the working and common electrodes connected along the sides of the cell at the terminals and sense leads attached to the tabs in the middle of the cell.

Figure 15. Photographs of the Toshiba cells set up for initial characterization from the PGSTAT302N.

Using the characterization data, the equivalent series resistance (ESR) was calculated using the following equation:

$$ESR = \frac{[0.5C]V - [XC]V}{[XC]A - 11.5A} \quad (2)$$

This equation compares the voltage at higher rates of continuous current discharge to the voltage and current at 0.5C. Equation 2 is representative of the calculation performed for a 23 Ah cell where 0.5C is equal to 11.5 A. By performing this calculation, a plot of the ESR can be calculated and plotted as a function of percent depth of discharge. While it is not a very effective calculation at the endpoints of capacity where large changes in

voltage are seen, it is a useful measurement between 10% and 90 % SoC of the cells. This is represented by a more uniform region in the curve between these two points.

After initial characterization using EIS, the cell is connected to the single pulsed discharge testing stage. As described earlier, a unique low impedance testbed that is capable of discharging cells at pulsed currents as high as 10 kA was used. The load is shown photographically in Figure 16. In short, the stand works by discharging the cell under test into a series of sixty high power MOSFETs that are all connected in parallel. Each MOSFET has an on-state impedance of roughly 8 mΩ equating to an equivalent resistance of roughly 135 μΩ. The series connection of the MOSFETS with the other bus work that makes up the stand creates a load impedance that varies between 800 μΩ and 1000 μΩ. This is on the order of the impedance of the cells being tested meaning that near matched load impedances can be evaluated. Though the stand can be tuned using externally variable bus work, no tuning occurred in the experiments performed here.

Additional copper bus work is attached to the terminals of the cell to serve as a junction between the cell and the ring terminal of the testbed cable. When pulsing the cell under test, its voltage is measured using a differential voltage monitor and its discharge current is measured using a CWT Rogowski coil, both of which can be seen in the images below. Along with being responsible for controlling the MOSFETs switching frequency, LabVIEW is used to record the voltage and current using a PXI chassis data acquisition system. As already described, each cell was pulse discharged for 200 ms into the lowest impedance possible. By taking the initial change in voltage as it transitions from an open circuit potential to a conduction potential, and dividing that change by the current

measured, the internal impedance of the cell can be characterized under high current, pulsed DC conditions.

Figure 16. The single pulsed discharge experimental testbed (left) and a Toshiba cell (right) firmly connected using 3/0 copper welding cable and additional bus work attached to the cell.

3.3.3 Continuous Duty Cycle Characterization

As previously stated, Chroma 63209 programmable loads and Sorensen power supplies are used to load and recharge the cells and modules when they are repetitively pulse cycled. The programmable load and supplies are connected to a central bus using 3/0 copper welding cable. Another set of cables extend from the central bus and into the temperature chamber where they are connected to the cell for repetitive pulsed testing. A thermocouple is placed on the body, the cathode, and the anode of each cell and another is set freely inside the temperature chamber for ambient temperature measurement. The cells required bus work to establish a junction between the ring terminal of the cabling and the

terminals of the cell. Photographs of the cell set up for repetitive pulsed testing can be seen in Figure 17.

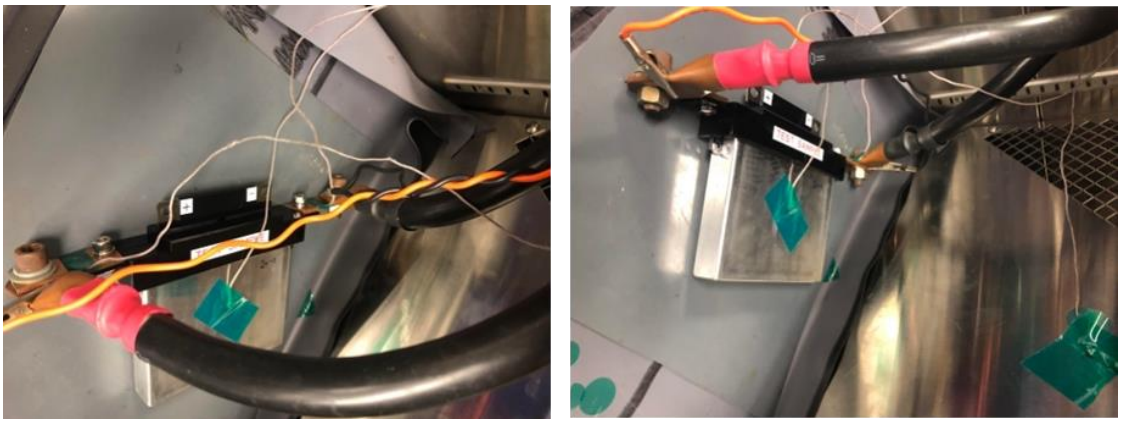

Figure 17. Sample photographs of the Toshiba cells prior to evaluation showing both the terminals and their connection to bus work.

3.3.4 Capacity Fade Measurement through Repeated Cycling

The last series of tests conducted on the cells was aimed at studying the capacity fade of each cell type. Once the cell under study has undergone the initial characterization procedure, it is placed in a temperature chamber, held at 20°C, and is subjected to cycling. The cycling was conducted using a three different pulsing profiles. Pulsing was performed at a constant power rate that was calculated for each cell based on the conduction voltage of that cell and the operational power each battery would require if it were sized for a 1 kV open circuit potential and used to source 300 kW to a load. After calculating the constant power requirement, the lifetime cycling of each cell is broken into fifty cycle segments with each fifty cycles consisting of the following pulse profiles:

1. 10 cycles at 5 seconds on/5 seconds off at Max CP until V = Min V

   Recharge between each cycle is at MaxC – CC until V = Max V

   Last recharge is at Max C – CC/CV until Max V and C < 0.3 A

2. 10 cycles at 5 seconds on/1 seconds off at Max CP until V = Min V

   Recharge between each cycle is at MaxC – CC until V = Max V

   Last recharge is at MaxC – CC/CV until Max V and C < 0.3 A

3. 10 cycles at 5 seconds on/5 seconds off at Max CP until V = Min V

   Recharge between each cycle is at MaxC – CC until V = Max V

   Last recharge is at MaxC – CC/CV until Max V and C < 0.3 A

4. 10 cycles at 30 seconds on/5 seconds off at Max CP until V = Min V

   Recharge between each cycle is at MaxC – CC until V = Max V

   Last recharge is at MaxC – CC/CV until Max V and C < 0.3 A

5. 10 cycles at 5 seconds on/5 seconds off at Max CP until V = Min V

   Recharge between each cycle is at MaxC – CC until V = Max V

   Last recharge is at MaxC – CC/CV until Max V and C < 0.3 A

Constant power was calculated for each cell by calculating the operational power each battery would operate at if it were sized for a 1 kV open circuit potential and used to

source 300 kW to a load. The number of series cells was determined by dividing 1 kV by the maximum voltage of each of the cells. Then, the 300 kW load is divided by the multiplication of the number of cells in series and the anticipated conduction voltage per cell. This conduction voltage is determined from the higher capacity constant current discharges obtained during the initial characterization of each cell. The number of parallel cells are then determined by dividing the current required by the maximum current a series string of cells can source. The constant power for each cell is calculated by dividing the 300 kW by the number of cells in series and parallel. Table 3 shows a summary of the results obtained using this calculation procedure and the resulting constant power used for this testing procedure.

Table 3. Characteristics of battery system sized for a 1 kV open circuit potential and used to source 300 kW to a load.

Cell	Minimum Voltage [V]	Maximum Voltage [V]	Constant Power Discharge [W]	Constant Current Recharge [A]	Cut-off Temperature [^{o}C]
10 Ah	1.8	2.8	220	110	55
23 Ah	1.5	2.7	200	100	55

This testing was performed inside the Espec programmable temperature chambers using a Sorenson power supply and a Chroma 63209 load as shown in Figure 18. The power supply and load were connected to a common bus bar which was then routed into the temperature chamber using 3/0 cable. The cell was outfitted with additional bus work to allow connection of the cell to the ring terminals of the cables. This was previously demonstrated in Figure 17.

Figure 18. Photograph of the Espec programmable temperature chambers (left) and the power supplies and loads (right).

3.4 Experimental Results

Each of the four previously described tests were performed on the three respective cell types to determine operational characteristics and aid in the development of a mathematical model for these cells.

3.4.1 C Rate Characterization

The usable capacity of each cell was measured by first performing symmetric charging and discharging at multiple rates determined by the manufacturer's datasheet, and the data collected for each cell was used, along with Equation 2, to calculate the ESR as a function of depth of discharge (DoD). After each cell was subjected to 2500 cycles, the same procedure was followed. The results for each cell are shown below in Figure 19 for a Toshiba 10 Ah cell and Figure 20 for a Toshiba 23 Ah cell. This comparison shows the effect of aging on each of these cells by observing the difference between the baseline for each cell's capacity during discharge and ESR before testing to that after cycling.

According to the discharge curves, the Toshiba cells exhibit a near linear decrease in voltage during much of the discharge cycle.

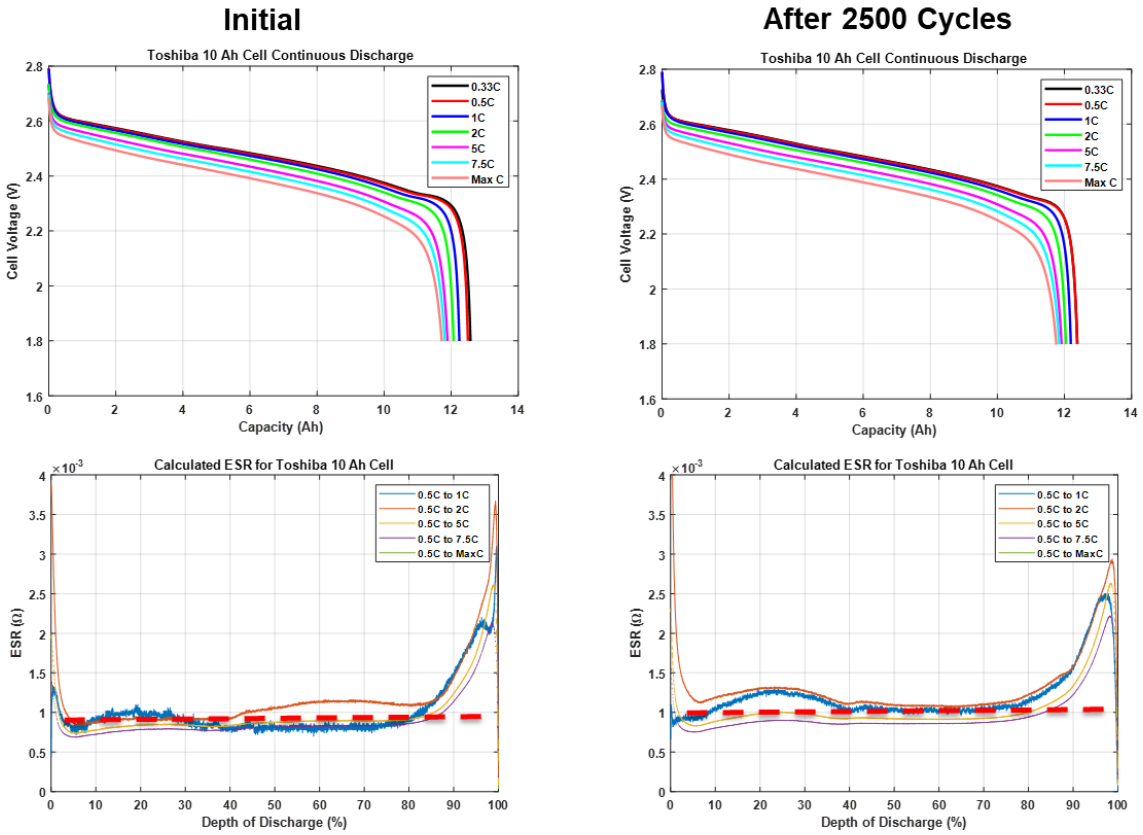

Figure 19. Cell capacity during multiple continuous discharge cycles and calculated ESR before cycling (left) and after cycling (right) for a Toshiba 10 Ah cell.

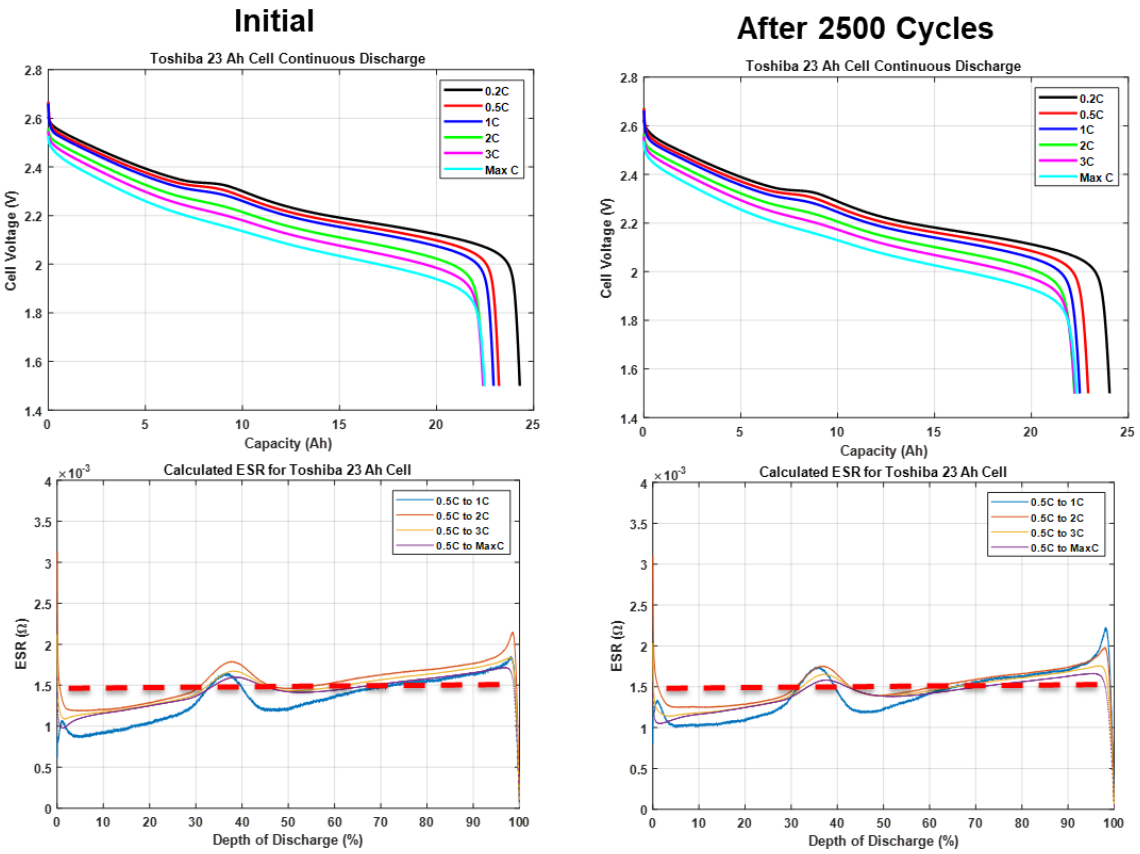

Figure 20. Cell capacity during multiple continuous discharge cycles and calculated ESR before cycling (left) and after cycling (right) for a Toshiba 23 Ah cell.

During each continuous charge/discharge cycle, the cell's body temperature was monitored using a thermocouple placed in the middle of the cell body. The temperature rise during each individual charge/discharge cycle for each cell under test is reported in Figure 21. According to the collected data, none of the cells reached or exceeded their thermal limits during any of the charge/discharge cycles.

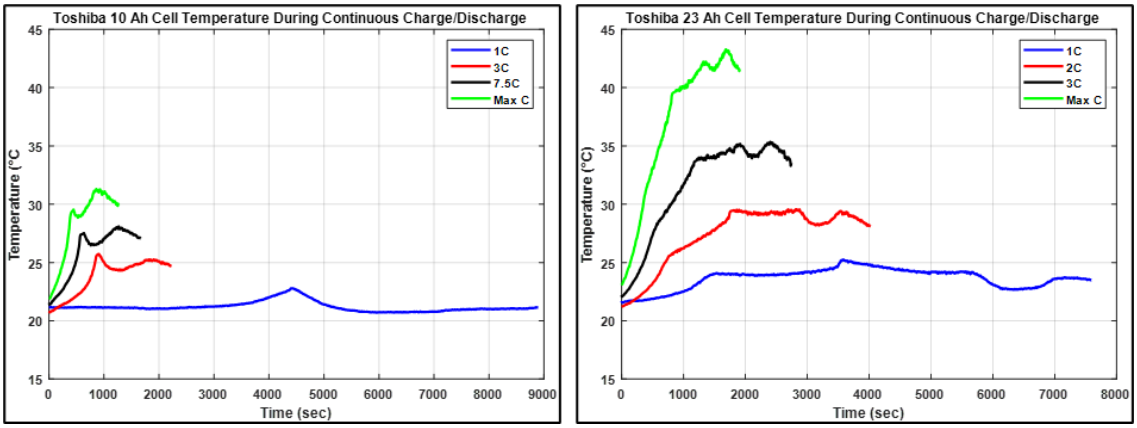

Figure 21. Cell temperature rise during each charge/discharge cycle for each cell under test.

3.4.2 Impedance Measurement

EIS profiles are used to speculate on how a cells' impedance changes as a function of aging as well as its charge voltage. Figure 22 shows the EIS data for the Toshiba 10 Ah cell and Figure 23 shows the data for the Toshiba 23 Ah cell. Analysis of the EIS data collected shows little change in each cells' impedance as a result of lifetime cycling.

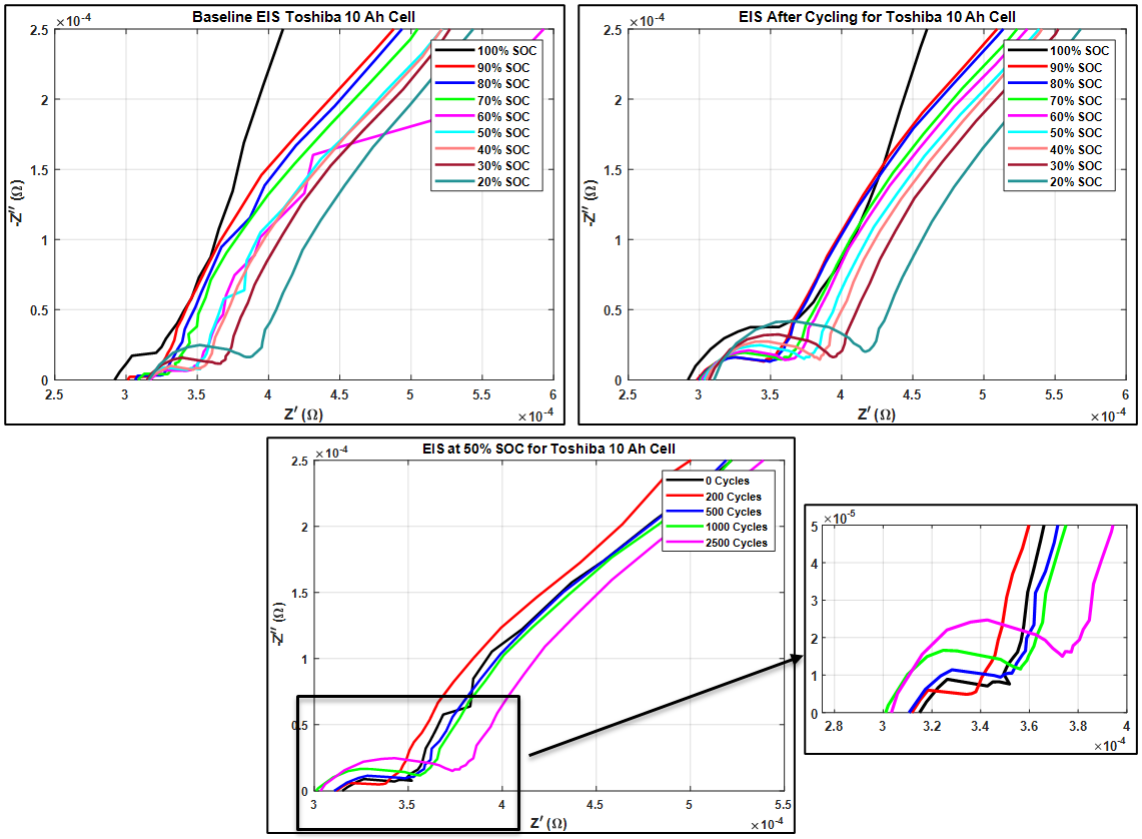

Figure 22. Electrochemical impedance spectroscopy (EIS) measurements made from the Toshiba 10 Ah cell as a function of their charge voltage in 10% increments.

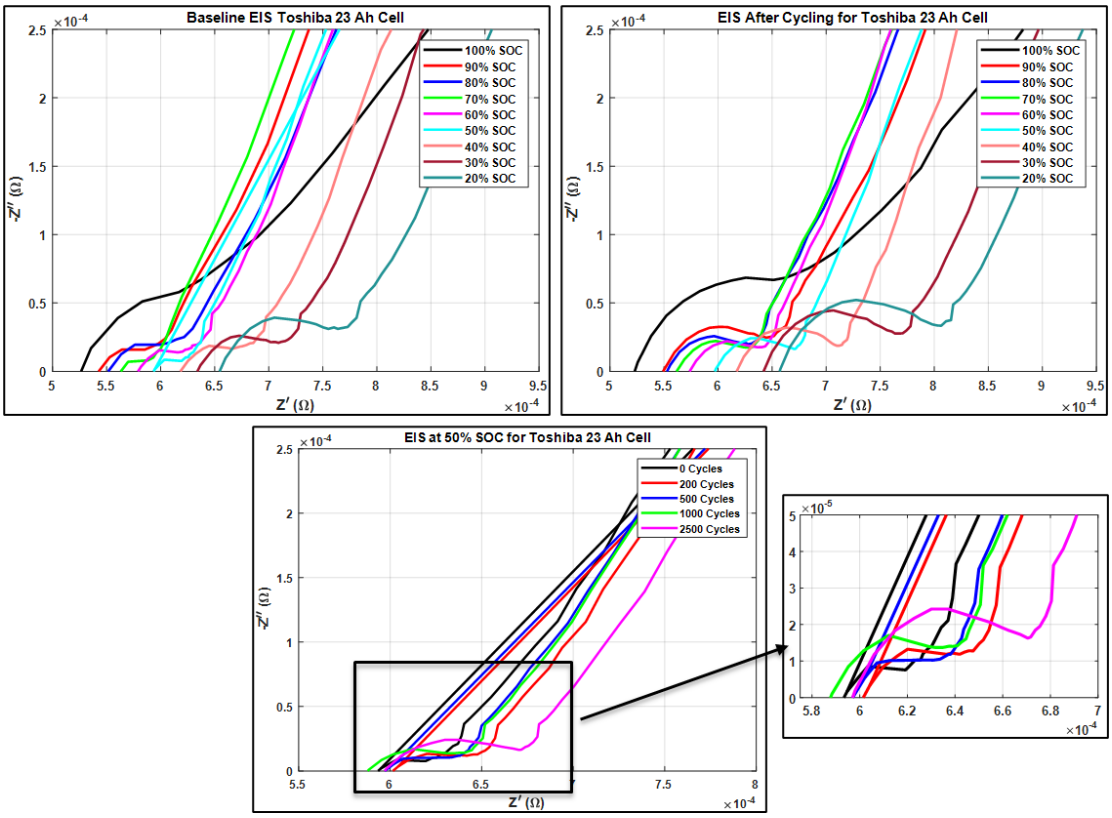

Figure 23. Electrochemical impedance spectroscopy (EIS) measurements made from the Toshiba 23 Ah cell as a function of their charge voltage in 10% increments.

The next series of results presented are those collected when each type of cell was discharged for 200 ms into a low impedance load using UTA's custom discharge stand. This experiment was aimed at further characterizing each cells' DC impedance when conducing high current as well as measuring their power density into near matched loads. Figure 24 presents the conduction voltages (left) and the conduction currents (right) measured from each respective type of cell. The impedance is measured by subtracting a cells' conduction voltage from the open circuit potential prior to conduction. Dividing the voltage drop measured by the conduction current results in an accurate estimate of the cell's

internal DC resistance. A higher conduction voltage and higher pulsed current equates to a cell with a lower internal resistance.

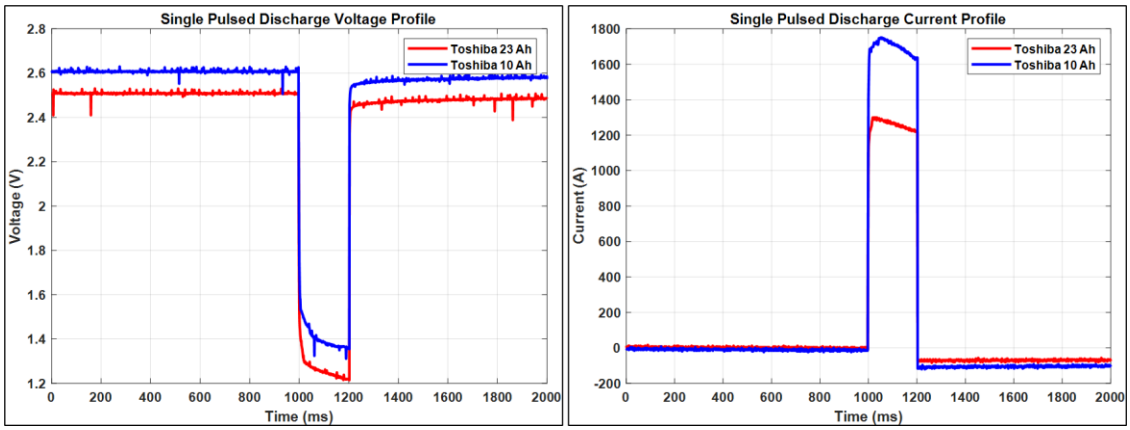

Figure 24. Single pulsed discharge voltage profiles for each of the cells (left) and their corresponding current profiles (right).

The Toshiba 10 Ah cell was discharged into a 0.808 mΩ load impedance supplying a peak current of 1.718 kA, and the cell's impedance was calculated to 0.712 mΩ. The Toshiba 23 Ah cell was discharged into a 1.100 mΩ load impedance supplying a peak current of 1.264 kA, and the cell's impedance was calculated to 0.993 mΩ. The calculated impedance values for each cell align well with the value stated in the manufacturer's datasheet.

3.4.3 Continuous Duty Cycle Characterization

Each cell was continuously cycled between 90% and 40% SoC at various charge/discharge rates, and a thermocouple was placed at the center of the body of each cell to measure the rise in body temperature during this continuous charge/discharge

cycling. This procedure was performed in a temperature chamber at 20°C and the observed temperature rise on each cell is shown in Figure 25. Each cell was observed to have a temperature rise on the body of the cell before reaching a point of thermal equilibrium, after which there was no additional temperature rise.

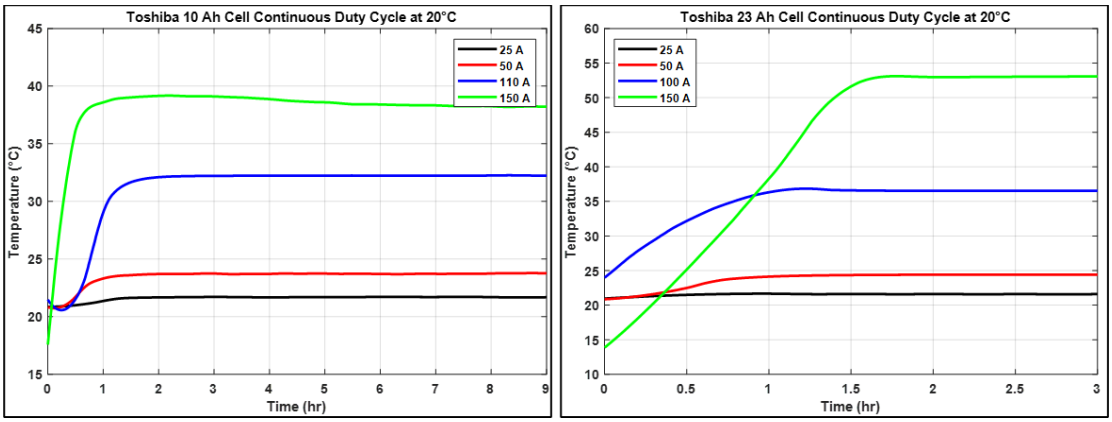

Figure 25. Thermal data during continuous duty cycling of a Toshiba 10 Ah and 23 Ah cell at 20 °C ambient temperature.

Table 4 contains a summary of the operational characteristics of each cell determined by the testing performed.

Table 4. Load impedance, peak current, and calculated cell impedance for each LTO cell

Parameter	10 Ah	23 Ah
Maximum Capacity	12.28 Ah	23.22 Ah
Load Impedance	0.808 mΩ	1.100 mΩ
Cell Impedance	0.712 mΩ	0.993 mΩ
Peak Current	1.718 kA	1.264 kA
Temperature During Continuous Duty Cycle	40.53°C	54.80°C

3.4.4 Capacity Fade Measurement through Repeated Cycling

The following results are collected from each type of cell when subjected to repetitive pulsed cycle testing. These tests are conducted to determine how each type of cell will perform electrically and thermally when subject to the cycling profile previously described. Figure 26 shows a sample of the electrical and thermal data gathered for each cell when subject to the cycling test procedure. The voltage profiles give insight to how each cell will perform when subject to a repetitively pulsed load.

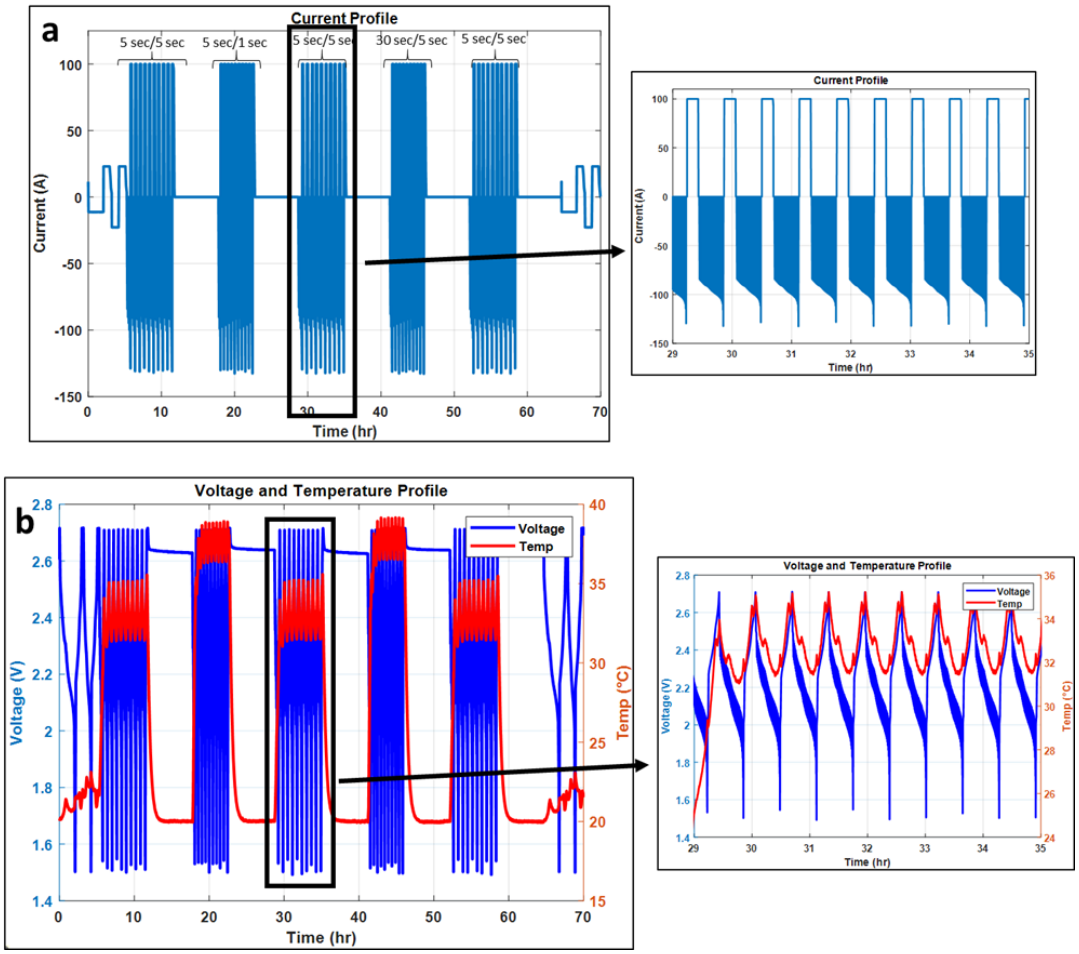

Figure 26. Sample electrical and thermal data for one cell undergoing lifetime cycling.

After each fifty cycles, the cell was re-characterized using a 1C and 0.5C charge/discharge rate. The voltage and capacity were recorded during continuous discharge and these discharge profiles were plotted together to show the change in capacity because of lifetime cycling. This change in capacity for each cell over the 2500 cycle period is shown in Figure 27 and numerically in Table 5.

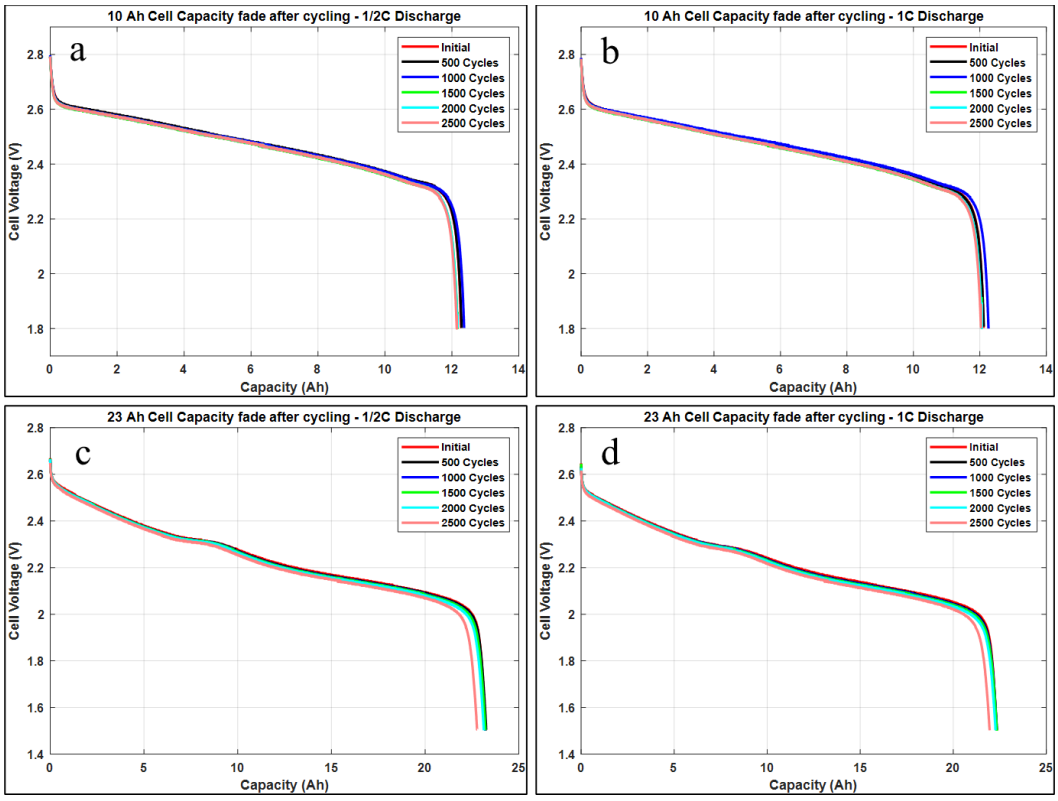

Figure 27. Change in capacity after 2500 cycles at (a,c) 0.5C and (b,d) 1C for each cell.

Table 5. Recorded capacity before and after cycling

Cell	Capacity at 0.5C Discharge			Capacity at 1C Discharge		
	Initial [Ah]	After 2500 Cycles [Ah]	Difference [%]	Initial [Ah]	After 2500 Cycles [Ah]	Difference [%]
10 Ah	12.275	12.145	1.06	12.245	12.034	1.72
23 Ah	23.224	22.772	1.95	22.330	21.954	1.68

Figure 27 illustrates and Table 5 documents that the amount of capacity fade among these LTO cells is minimal within a 2500 cycle lifetime. The 23 Ah cell exhibits the most capacity fade when baselined at 0.5C and 1C but is still below 2% followed by the 10 Ah cell. Assuming that these cells are cycled at a rate of one cycle per day, this accounts for approximately six and a half years of lifetime use and exhibit little to no capacity fade during this time. Keep in mind that this estimate does not account for calendar aging.

3.5 Mathematical Modeling

Two different methods were used to model the characteristics of the LTO cells:

1. Randles circuit
2. Average value model.

3.5.1 Randles Circuit

Although there is only a minimal change in capacity observed, EIS was performed before testing and then periodically throughout the cycling process to serve as a means of characterizing the electrochemical properties of the cell. These profiles are used to speculate on how a cells' impedance changes as a function of aging as well as its charge voltage. This initial and final EIS data was fitted to an electrochemical circuit, which is shown in Figure 28, along with the Nyquist plots for each cell at 50% SOC.

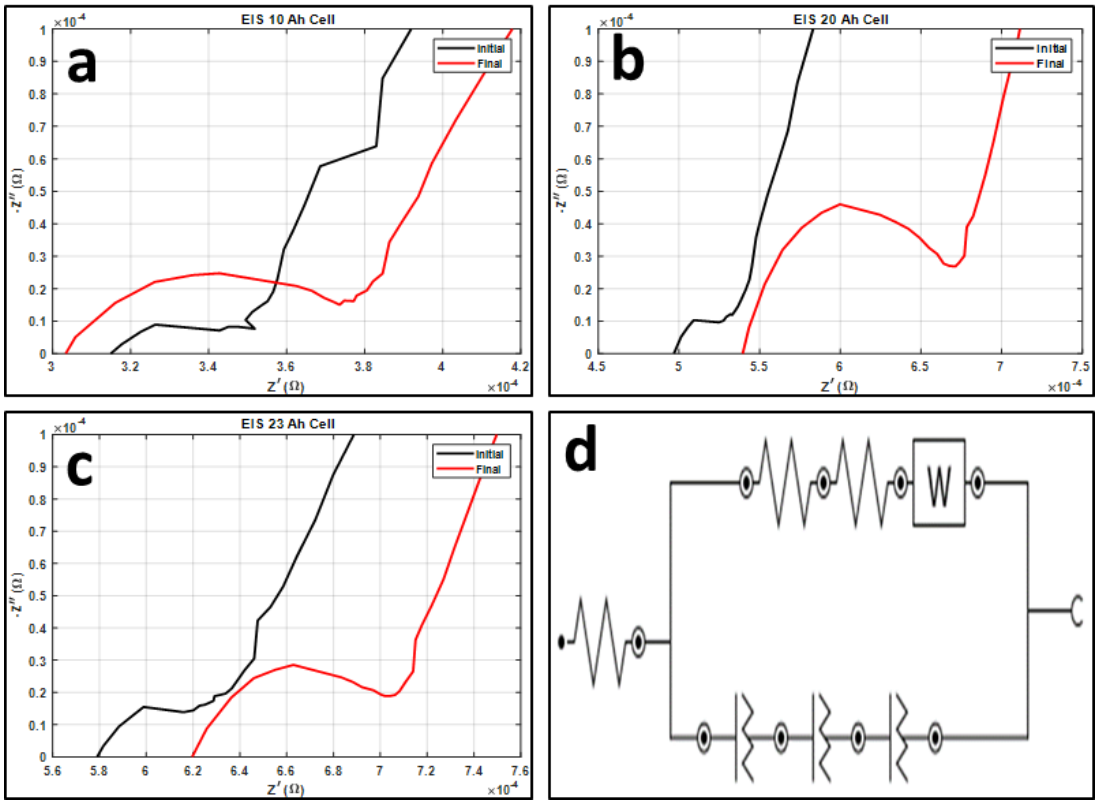

Figure 28. Electrochemical impedance spectroscopy for LTO cells where EIS was performed on a (a) 10 Ah cell, (b) 20 Ah cell, and a (c) 23 Ah cell at the beginning and at the conclusion of cycling. (d) This data was then fitted to an electrochemical circuit.

Each cell was initially fitted using a Randles circuit, which is intended to characterize the high frequency FRA data and the electron transfer within the cell. Figure 28 shows that there are obvious differences that exist within this region for each of the cells; however, the Warburg impedance, which represents the low frequency region of the Nyquist plot, was the basis of comparison in this study. The Warburg impedance, W, for each cell initially and after cycling is listed below in Table 6.

Table 6. Warburg impedance values before and after cycling

Cell	Initial Warburg Impedance	Final Warburg Impedance
10 Ah	7.77 kMho-$s^{1/2}$	8.25 kMho-$s^{1/2}$
23 Ah	7.21 kMho-$s^{1/2}$	7.60 kMho-$s^{1/2}$

These values show that there is some increase in the Warburg impedance in the 23 Ah and 10 Ah cells because of the cycling process indicating an increase in the resistance to slow diffusion within the cell. Conversely, the 20 Ah cell exhibits a decrease in the Warburg impedance between initial EIS and EIS after cycling which possibly correlates to the lack of observed change in capacity within this cell during the cycling process. This along with changes in the electrolyte and electrodes over time most likely leads to the capacity fade observed within the cells but it is much slower in this chemistry than what is observed in other lithium-ion chemistries which leads to the longer cycle life for LTO cells.

3.5.2 Average Value Model

The characterization data for the 10 Ah and 23 Ah LTO cell was used to create an average value model where the voltage is set as the variable with respect to the cell's capacity and discharge current, V([Ah],[A]). The *Gridfit* function within MATLAB was

used to interpolate and extrapolate between the input characterization data and create surface plots with respect to the previously mentioned variables. These surface plots are shown in Figure 29 for the 10 Ah and 23 Ah cells.

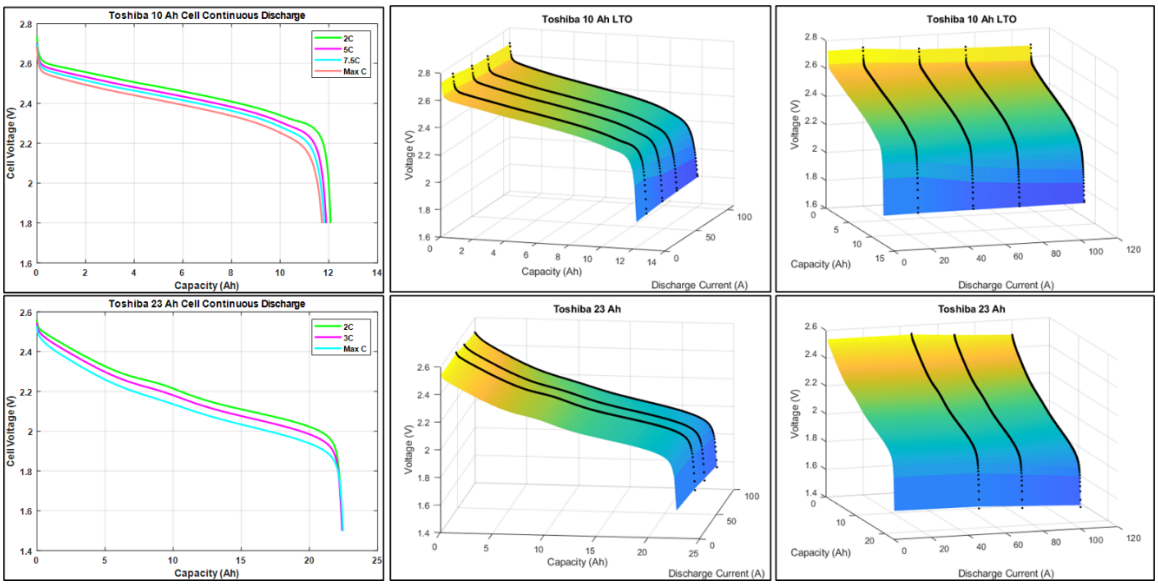

Figure 29. Surface plots generated for a 10 Ah and 23 Ah Toshiba LTO cell using MATLAB.

While electrochemical modeling using the Randles circuit technique is beneficial for understanding the electrical elements of a cell, the average value method provides the capability of using the characterization data to simulate an LTO battery without procuring the necessary cells. Figure 30 shows the surface plots produced using the characterization data and MATLAB to create a 1 kV equivalent battery consisting of either 420 10 Ah cells or 440 23 Ah cells. These surface plots, along with the TDK installed in the testbed, can be used to simulate the characteristics of a 1 kV LTO battery and study the differences between this technology and the 1 kV Saft battery already installed in IDEAL.

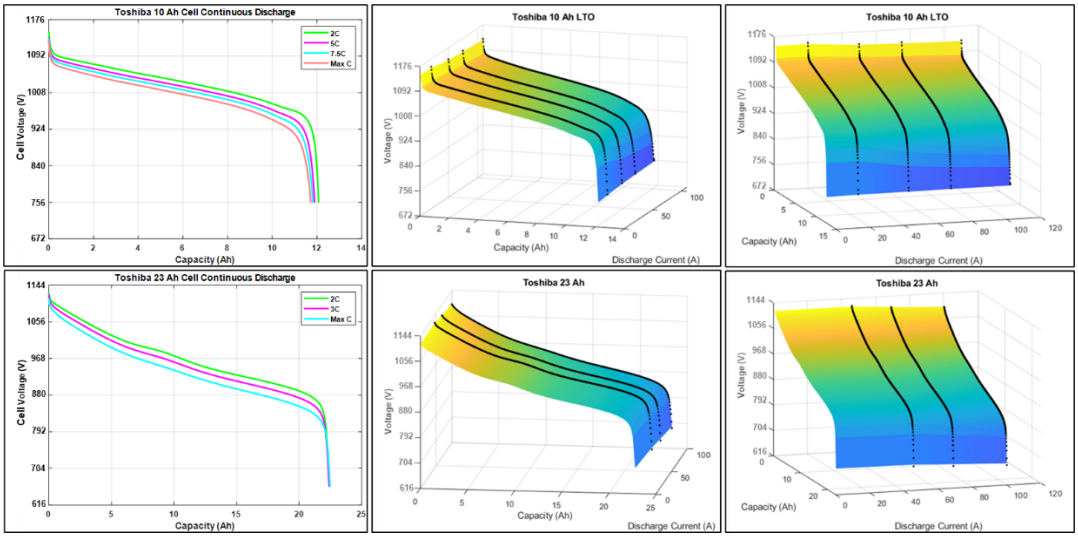

Figure 30. Surface plots generated for a 10 Ah and 23 Ah Toshiba battery.

Chapter 4

MOTOR GENERATOR STUDY

The first electric generator was developed in 1831 by Michael Faraday as a means of producing electricity through the rotation of a disk. Continued research has led to the development of modern-day generators that supply electricity to the power grid and motors that can be utilized in various mechanical and electrical applications. As this technology advanced, it was realized that these generators could be used aboard ships effectively converting them from the traditional wind or steam powered method of sailing to an electric driven system [1-4].

The UTA IDEAL testbed, Figure 4, was designed to incorporate these rotating machines as a prime source of power generation for studying the impact that varying levels of AC and DC loads in either constant or pulsed power operation have on these components. In the testbed, there is one three-phase AC machine that serves as the primary source of power which then branches out from the 480 VAC bus and then there is a separate nine-phase machine that is rectified to 1 kVDC that supports the 1 kVDC bus. This study focuses on testing and modeling of each of these machines using loads currently available in the testbed and applicable verification and validation procedural techniques previously described.

4.1 Three-Phase Generator

Within the IDEAL testbed, at the far left of Figure 4, is a variable frequency drive (VFD) controlled electrical M-G set, procured from KATO Engineering. The generator

supplies three phase, 480 VAC to the testbed and acts as the primary source of power under normal operation. The M-G set utilizes a 300 HP four-pole induction motor to spin a four-pole synchronous generator to 1500 – 2000 RPM. The motor is energized using a VFD through a 400 A electrical feed supplied at 480 VAC. The generator is excited using a direct contact brushless exciter.

As already described earlier, KATO designed the generator to allow for the amplitude of its output voltage and its output frequency to be adjusted remotely by the user using two respective analog control signals. The voltage is variable from -20% (384 VAC) to +20% (576 VAC) of the nominal 480 VAC using a 0 – 10 V analog signal. The output frequency is adjustable from -17% (50 Hz) to +11% (67 Hz) of the nominal 60 Hz using a second 0 – 10 V analog control signal. In this effort, considerable time was spent putting this motor-generator set through a modeling and then a V&V process to evaluate the model. The V&V process begins by determining the experimental conditions that constrain the applicability of the model and then determining the level of accuracy required of the output variables within the model according to its specified purpose. Requirements for the motor/generator set were determined using the standards found in MIL Spec 1399-300B [43] for a Type I generator operating at 480 V and 60 Hz and are shown in Table 7.

Table 7. MIL Spec 1399-300B [43] requirements for a Type I generator operating at 480 V and 60 Hz.

Parameter	Tolerances			Allowances	
	Lower Limit	Nominal	Upper Limit	Transient Condition	Worst-Case Excursion
Voltage	447 V	480 V	513 V	± 16%	± 20%
Frequency	58 Hz	60 Hz	62 Hz	± 4%	± 5.5%

4.1.1 Model Development

The motor/generator set was modeled in a Simulink® workspace using a per unit fundamental three-phase synchronous generator block, located in the Simscape library, and an IEEE AC1A exciter system for control of the field voltage. The parameters for the three-phase generator are listed in Table 8.

Table 8. Three-phase synchronous generator model parameters.

Variable	Description	Value
S	Nominal power	166.7 kVA
V	Rated voltage (line-to-line, RMS)	480 kV
f	Rated frequency	60 Hz
X_d	d-axis unsaturated reactance	0.588 pu
X_d’	d-axis unsaturated transient reactance	0.082 pu
X_d’’	d-axis unsaturated sub-transient reactance	0.078 pu
X_q	q-axis unsaturated reactance	0.29 pu
X_q’	q-axis unsaturated transient reactance	0.322 pu
X_q’’	q-axis unsaturated sub-transient reactance	0.081 pu
R_s	Stator resistance	0.0029 pu
T_d’	d-axis unsaturated transient open time constant	0.238 sec
T_d’’	d-axis unsaturated sub-transient open time constant	0.017 sec
$T_{q''}$	q-axis unsaturated sub-transient open time constant	0.354 sec
H	Inertia coefficient	2.434 sec
F	Friction factor	0.084 pu
p	Pole pairs	2

The 300 hp induction motor-controller for this M-G set receives a 480 V input from the grid. Numerous studies have documented methods for developing a mathematical relationship for a motor that is either a gas turbine or diesel engine but there were no studies found during the literature review that documented methods for developing a controller that has an electrical input. Direct modeling of the VFD would require proprietary information from the manufacturer and could be computationally expensive; therefore, a proportional-integral controller methodology, shown if Figure 31, was developed and

implemented instead. Tuning the controller parameters was accomplished during the testing phase of the machine.

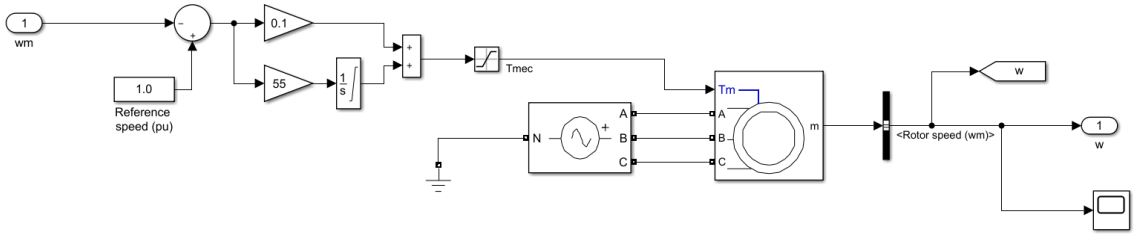

Figure 31. PI controller developed for the three-phase M-G set.

The open circuit voltage (OCV) of the generator was measured by connecting its output to a large resistance, wye-connected network. Once the OCV was verified, the output of the generator model was transiently loaded by a fixed resistance load. Assuming a bus voltage of 480 VAC, the load steps applied are intended to load the generator at steps of 15 kW, 30 kW, 50 kW, 75 kW, 100 kW, and 125 kW, respectively. These same loading conditions were applied to the actual hardware using the 350 kW rated Mosebach resistive load bank directly connected to the output of the 480 VAC motor/generator set. The voltage and current on the 480 VAC bus were monitored and the experimental results are compared against the model results. Because the load is purely resistive, minimal power factor and frequency fluctuations are expected. One method to directly test the M-G set's response under non-linear loading conditions is by loading the generator using the 1 kV TDK. This was performed as a method to observe the frequency fluctuation of the machine and the model's ability to predict this behavior using a power factor dependent load.

4.1.2 Model and Experimental Results

The three-phase synchronous generator was modeled using Simscape electrical components embedded within the Simulink® library. The modeling results are compared to actual hardware experiments performed under similar loading conditions to determine the accuracy of the results. Initially, the OCV of the generator model was overlaid with the actual OCV of the system to evaluate how the model's voltage matches the hardware's voltage during a no-load situation. Next a constant resistance load, chosen to result in a particular power dissipation, was transiently applied to the generator to observe the sag in the generator's output voltage under these conditions. Similarly, when the load was transiently removed, the generator's response was measured and compared with that of the model. The generator model, the hardware's OCV overlaid with the model's OCV, and an example of the transient step loading applied to the system are shown in Figure 32 (a-c), respectively. Figure 32 (b) shows that the OCV of the model closely reproduces the OCV of the hardware with only a small phase shift due to the initial start-up of the machine in Simulink®. Calculation of the cross-correlation between these two signals yielded a maximum correlation of 0.758 with a lag of 23 ms. Step-loading was then performed at increments of 15 kW, 30 kW, 50 kW, 75 kW, 100 kW, and 125 kW, respectively, in both simulation and hardware. The results from each of these experiments will not be shown here but those from the 15 kW, Figure 33, and 125 kW, Figure 34, transient loading events will be. Within those figures, there are plots showing the full experiment along with zoomed in views of the current and voltage at the time of loading and unloading, respectively.

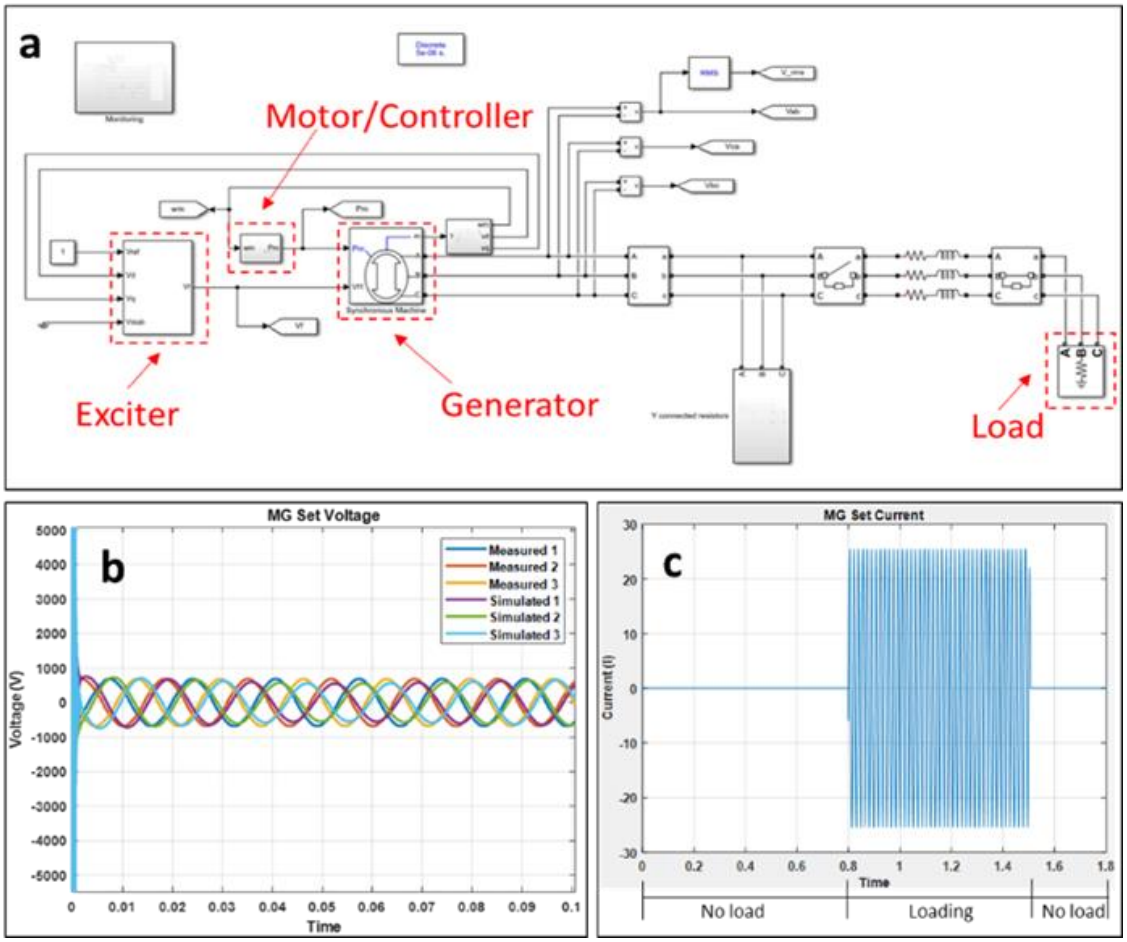

Figure 32. (a) A three-phase synchronous generator was developed in Simulink® with feedback for field voltage control and mechanical power control. The (b) OCV was measured and an example of (c) step loading with a 480 V constant power resistive load is shown.

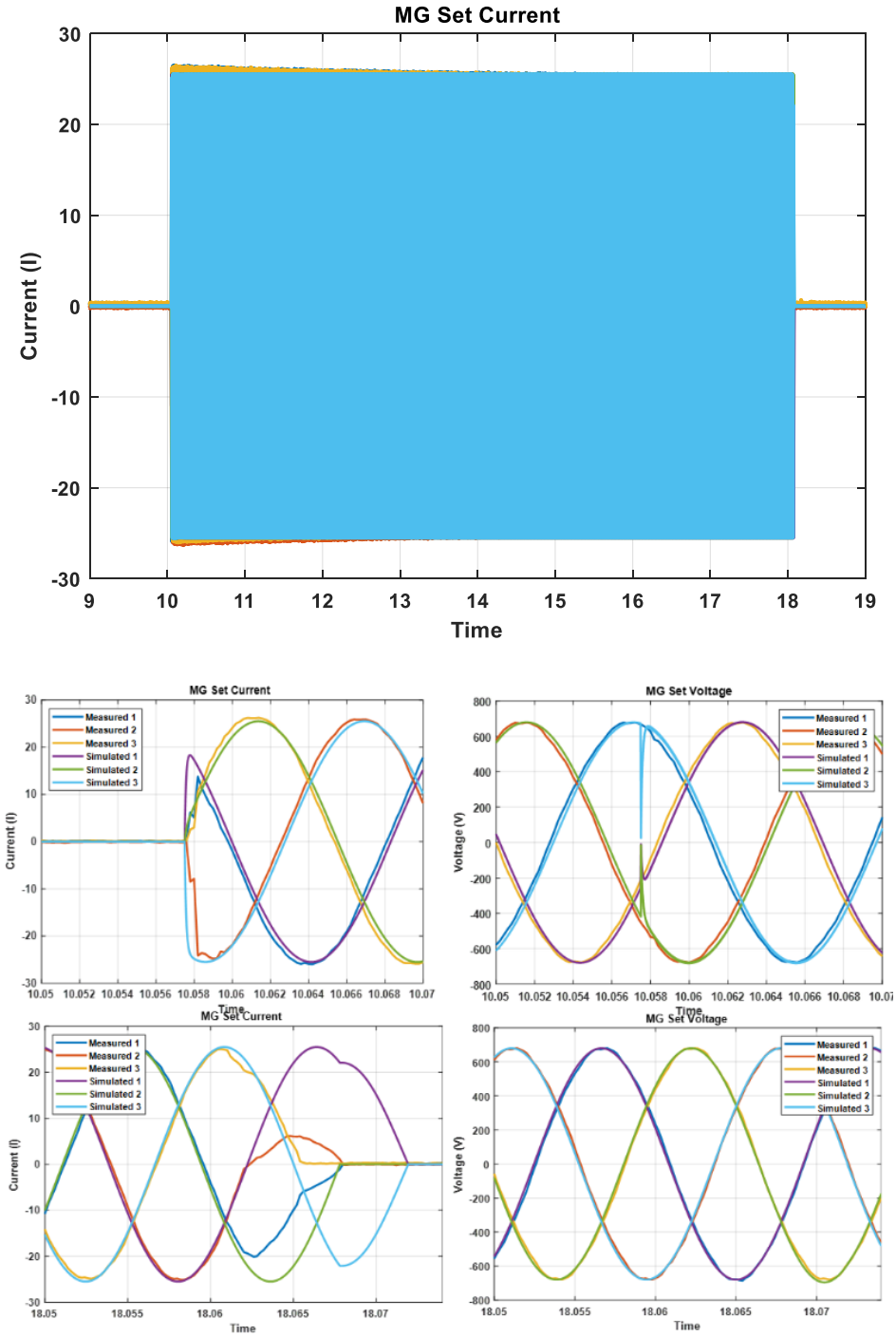

Figure 33. The Simulink® generator model was set to emulate a 15 kW transient load and was compared to the same results produced by hardware under the same testing conditions.

Evaluating the data, the transient response of the model closely represents the voltage observed in the hardware at the lowest and highest transient loads tested. There is some observed sagging and swelling at the moment of loading and unloading which becomes more pronounced as the load's power increases. Analysis of the RMS voltage indicates that the voltage does not exceed the upper and lower limits of MIL Spec 1399-300B under these loading conditions. To predict the load required to take the generator out of MIL Spec 1399-300B, the model was loaded slightly higher than those allowed by the actual hardware's rating. A plot of these loading conditions is shown in Figure 35. Table 9 lists the lowest and highest voltage value calculated by the model showing where the generator is predicted to exceed the bounds, indicated in red. From the model data in Figure 35 and Table 9, respectively, the model predicts that the generator's voltage will be unable to meet the MIL Spec 1399-300B during the unloading of approximately 225 kW and follows this trend until 300 kW where both the loading and unloading conditions exit allowed tolerances. There is little deviation expected in the frequency during these loading events since the load is purely resistive; however, slight frequency deviations are observed due to the change in torque and inertia of the machine.

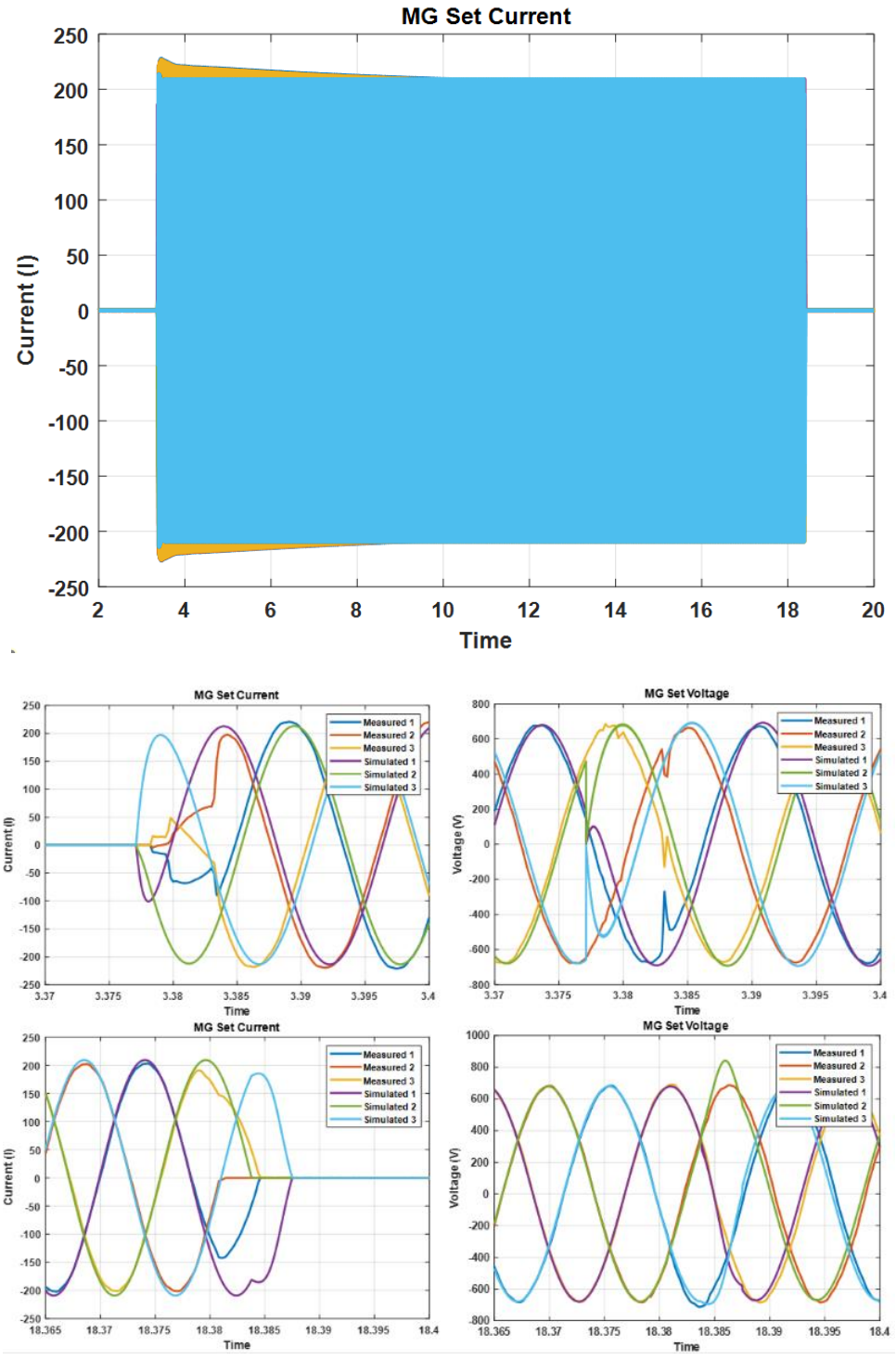

Figure 34. The Simulink® generator model was set to emulate a 125 kW transient load and was compared to the same results produced by hardware under the same testing conditions.

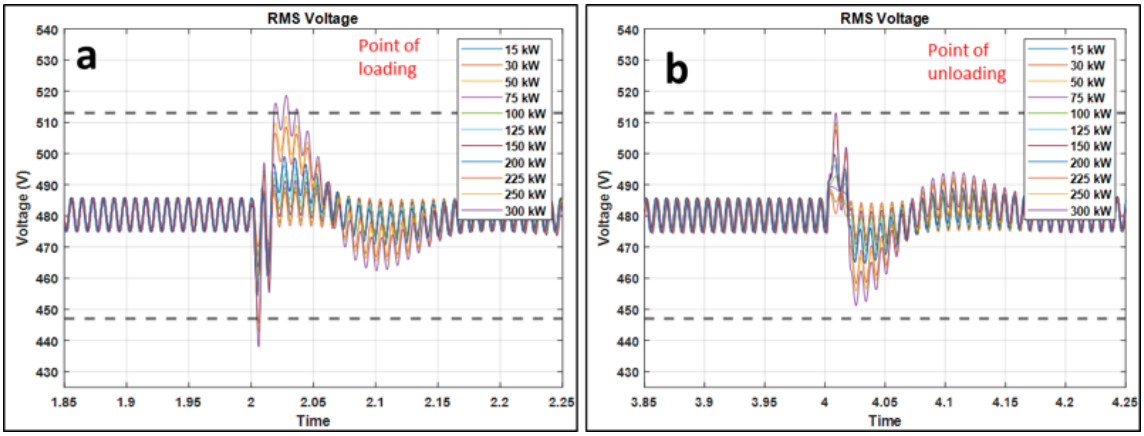

Figure 35. Modeled RMS voltage at time of (a) loading and (b) unloading for conditions when testing data is available and for conditions outside of hardware ratings capabilities. (Dashed lines correspond to the voltage values in Table 7.)

An FFT was performed at the time of loading and included the frequency content contained within a 1 sec window since MIL Spec 1399-300B specifies that frequency transients should recover within a 1 sec period. A comparison of the experimental and modeling FFT results for the same windows are shown in Figure 36 and they show good agreement, which was expected since these resistive loads do not represent non-linear transients that would cause sufficient harmonic injection. The FFT analysis of the voltage for the 15 kW, 125 kW, and 300 kW transient loading events, respectively, do not exceed any limits established in Table 7.

Table 9. Maximum and minimum voltages observed in simulation of a motor/generator set at different constant power transient loads.

Transient Step Load	Voltage Maximum [V]	Voltage Minimum [V]
15 kW	485.23	473.26
30 kW	487.85	470.10
50 kW	489.33	467.14
75 kW	491.35	463.64
100 kW	493.57	460.33
125 kW	496.38	457.55
150 kW	499.69	454.30
200 kW	505.31	448.28
225 kW	508.57	445.52
250 kW	511.93	442.88
300 kW	518.69	437.92

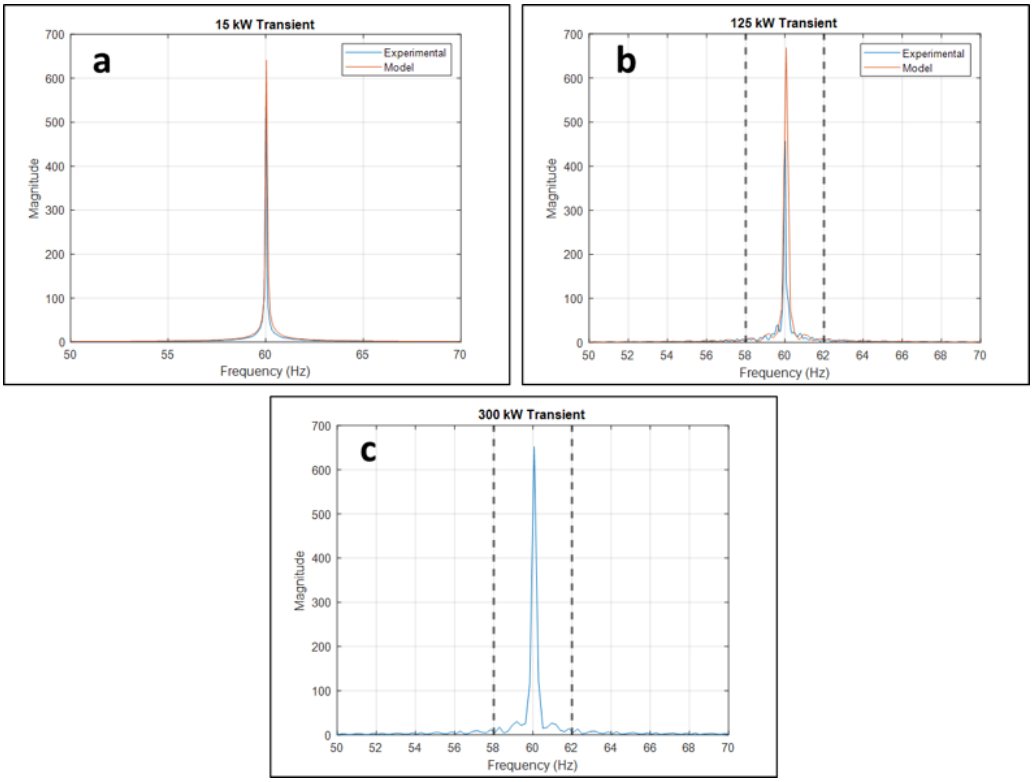

Figure 36. Frequency analysis (FFT) performed on simulated and hardware data during the time of step-loading for a (a) 15 kW load, (b) 125 kW load, and (c) 300 kW load. (Dashed lines correspond to the allowed frequency variance from Table 7.)

The Mosebach load used previously in this study is a variable resistance load and was shown to cause sag and swell during transient loading and unloading, respectively, but only

causes slight variations in frequency. This behavior is expected, therefore, the 1 kV TDK was used to provide a non-linear loading profile so that frequency variation can be observed. Figure 37 shows the results when the TDK was used to load the generator with 115 kW for 10 sec. In Simulink®, this non-linear load was modeled as a controlled current source using the source data from the TDK and the simulation and measured data at the time of loading is shown along with the frequency analysis for the window.

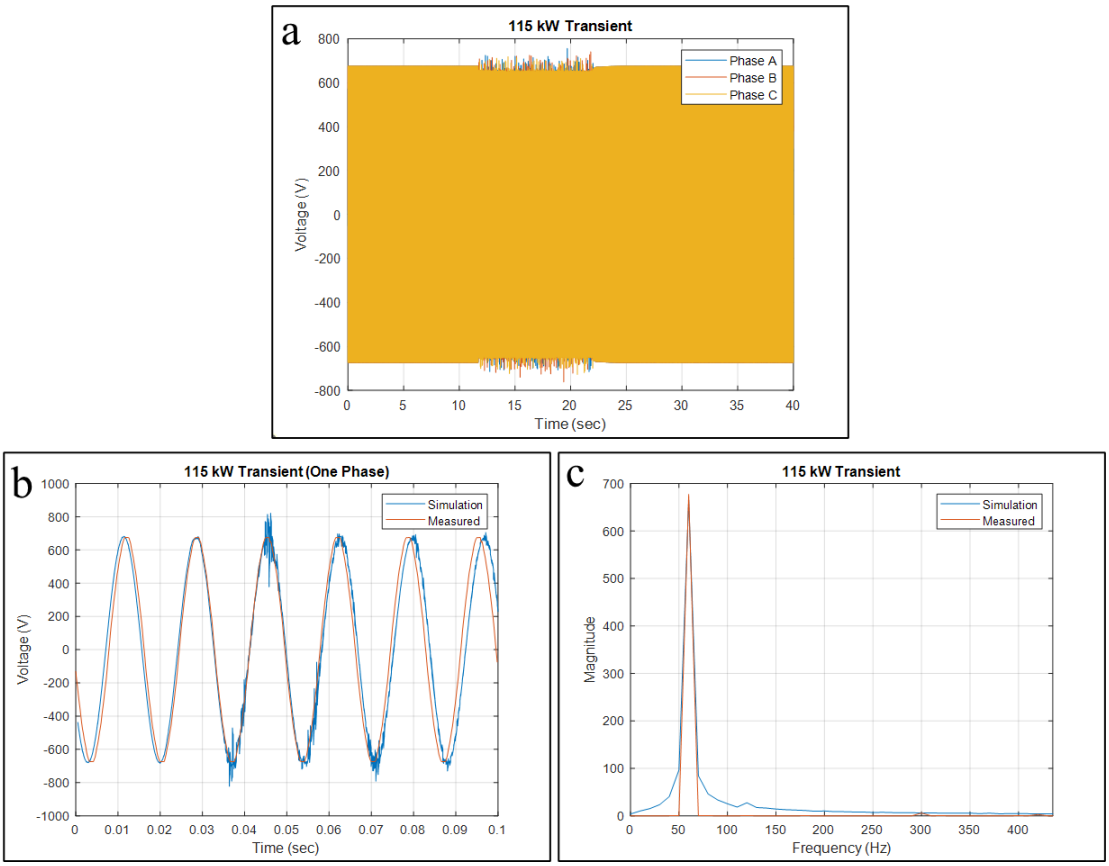

Figure 37. (a) Transient loading of the M-G set with the 1 kV TDK. (b) Measured and simulated voltage at the time of loading. (c) Frequency analysis (FFT) performed on simulated and hardware data during the time of step-loading.

These results show that Simulink® is an effective tool for modeling the frequency, voltage, and current characteristics of a three-phase generator and shows the limitations of the model under V&V and MIL-Spec 1399 guidelines. Additionally, this effort demonstrates that a PI controller can be substituted for a more complex VFD control structure when the specific details of that controller are unknown. Using this developed model, more complex simulations can be done with MVAC microgrid architectures where additional focus can be placed on frequency and synchronization issues which are inherent to those systems.

4.2 Nine-Phase Generator

It is difficult to integrate multiple generators onto a common AC bus. These prime movers must be synchronized, and the frequency of these machines must be adjusted to maintain the AC frequency at its required rating (i.e., 60 Hz) regardless of loading conditions [4]. This limits the ability to adjust and optimize the parameters of these machines as loads are stepped on and off and creates a less fuel efficient and more environmentally unfriendly solution. However, this can be overcome by introducing power electronic converters that rectify the AC power produced by the generator into a DC equivalent. Additionally, depending upon the voltage amplitude, DC power distribution systems provide a slightly easier opportunity for the inclusion of energy storage since it can be floated on the bus if the battery voltage and distribution voltage are well matched [5-6].

This effort focuses on the study of a motor-generator set that is rectified to 1 kVDC for supporting continuous and transient DC load profiles. 1 kVDC is the upper limit of

feasible battery potentials for use in zonal shipboard power systems. Therefore, direct integration of rectified motor-generator sets onto the 1 kVDC bus is advantageous. It should be noticed from the IDEAL testbed description that 1 kVDC is only produced in the testbed via either the programmable power supply or the battery, not from a motor-generator set directly. There are losses in additional power electronic supplies and controls challenges that can be avoided through direct rectification of the engine-generator onto the 1 kV DC bus.

A 40 kW, AC motor-generator was procured from KATO Engineering with a nine-phase AC output with an amplitude of roughly 711 VAC. The generator has an actively controlled AC/DC rectifier integrated on the output that rectifies the 711 VAC to ~1 kV DC. The motor is a 3 phase - 480 VAC electric motor that is run with a variable frequency drive. The frequency of the VFD is controllable between 110 Hz and 125 Hz using a 0 – 10 V analog control signal such that it can be used to emulate a diesel or gas-turbine generator model run on a hardware in the loop (HIL) platform. The generator has a nominally 120 Hz, 9-phase output at roughly 711 VAC and this voltage rectifies to approximately 1 kVDC. The output voltage of the generator can be varied by roughly 10% using a 0 – 10 V analog control signal. The nine-phase output of the generator is fed directly into an 18-pulse AC/DC rectifier that is actively controlled using silicone-controlled rectifiers (SCRs). Through modulation of the gate drivers, the rectifier output can be adjusted to produce a variable DC output voltage. This is shown conceptually in Figure 38. The motor-generator was studied in ways both independently and buffered using the battery installed in the UTA IDEAL testbed.

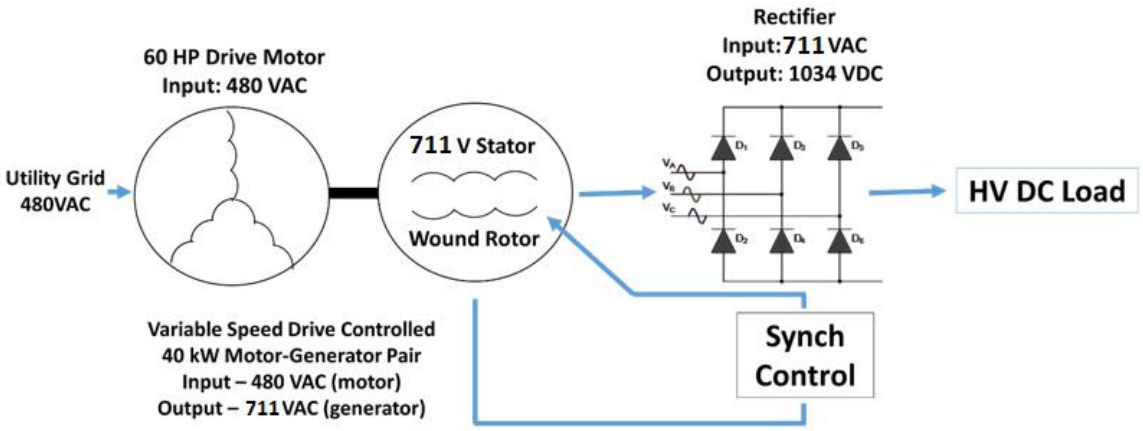

Figure 38. Simple concept drawing of the electric motor – generator / rectifier set.

4.2.1 Model Development

Simulink has a three-phase synchronous motor-generator model within its Simscape Electrical toolbox that was utilized for modeling the 150 kW, three-phase motor-generator set within the UTA IDEAL testbed. This three-phase model does not allow the user to adjust the number of phases within the machine or scale the model for machines with a higher number of phases. Therefore, a literature review was conducted into multiphase architectures to determine the parameters and equations required for the development of a nine-phase machine.

The literature review process determined that there is not currently a nine-phase model that has been developed and published using Simulink and validated against empirical data [44-63]. However, studies have been conducted on six-phase machines which include models, parameters, and collected data for comparison purposes. A six-phase synchronous generator model developed by Singh [44] was used as the basis for constructing this nine-phase machine. This model begins by developing a d-q

representation of the phase voltages and then developing an equivalent circuit within the d-q reference frame, shown in Figure 39 (a) and (b), respectively.

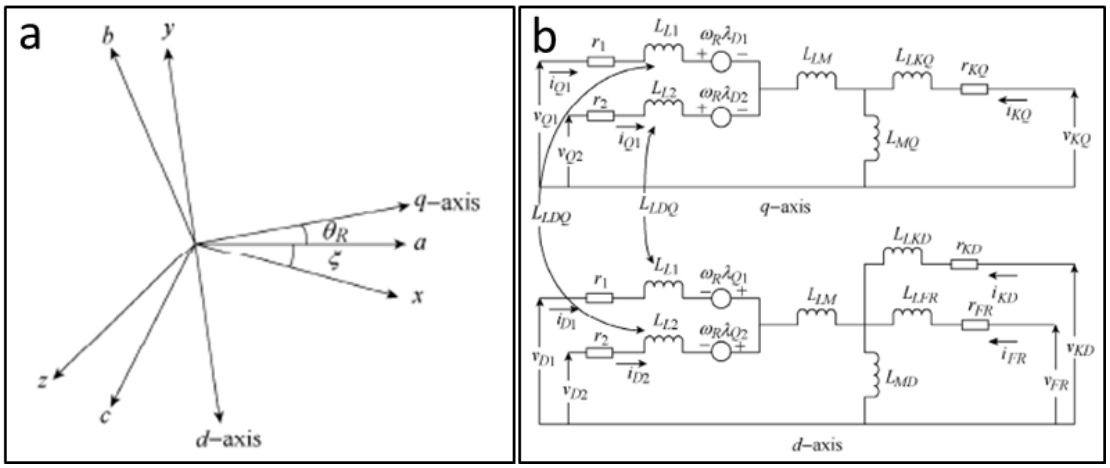

Figure 39. (a) The d-q representation of a six-phase synchronous machine and (b) it's associated equivalent circuit [44].

The methodology shown in Figure 39 was used to develop an equivalent circuit model in a nine-phase environment within the d-q reference frame, which is shown in Figure 40.

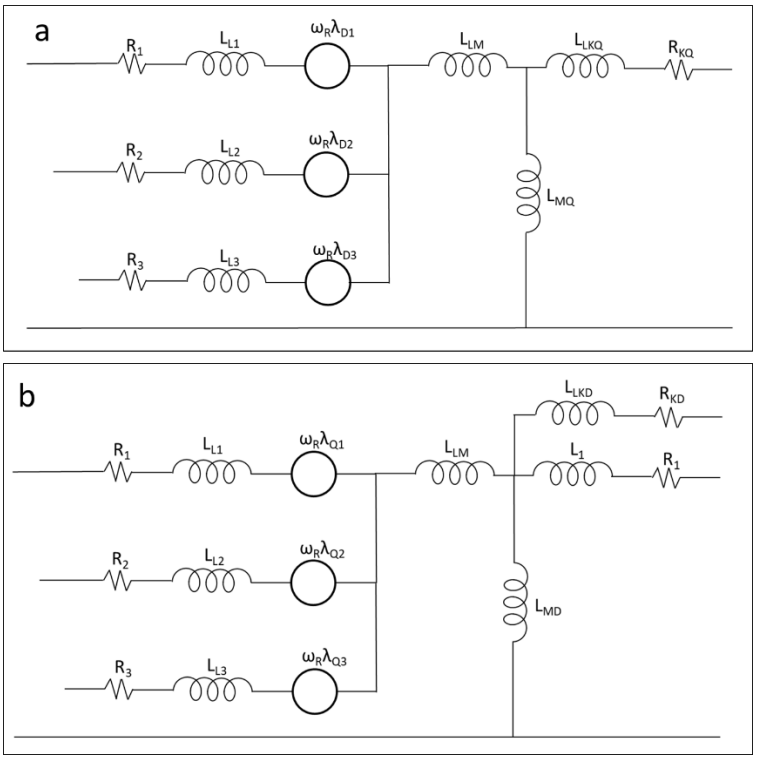

Figure 40. The equivalent circuit of a nine-phase synchronous generator in the (a) d-axis and (b) q-axis reference frames.

The equivalent circuit model in Figure 40 and the approach established in Singh's paper were the basis for developing the equations describing the electrical aspects of a nine-phase synchronous machine within Simulink, shown in Figure 41. This electrical section of the model consists of purely mathematical calculations with no Simscape or Simulink specific blocks.

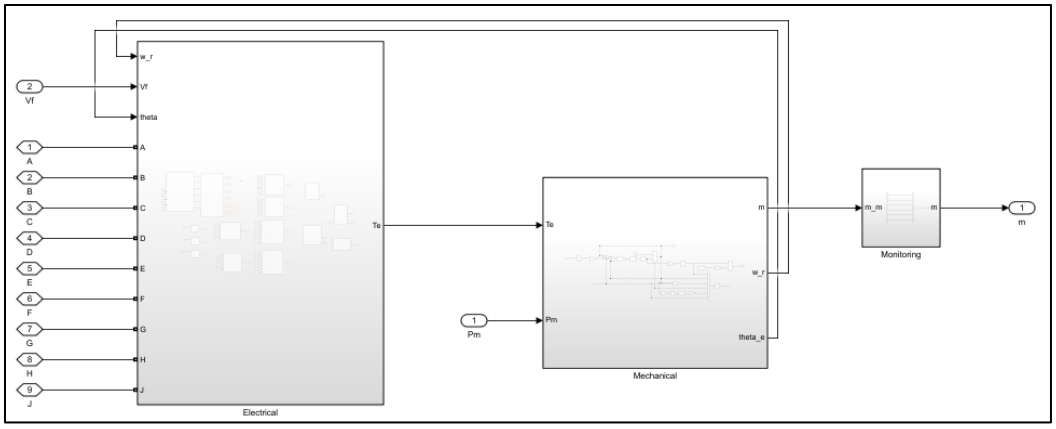

Figure 41. Top-level view of the Simulink model of a nine-phase generator. The model is divided into three sections: electrical model, mechanical model, and monitoring.

Within the electrical model, shown in Figure 41, there are multiple subsystems that were developed to perform the individual calculations related to the electrical nature of the system and the generator's equivalent circuit. The internal nature of the electrical subsystem is shown in Figure 42. The subsystem model shown in Figure 42 consists of four additional subsystems which function to either calculate currents that are fed back into the current injection subsystem or calculate the electrical torque that is fed through for calculation purposes in the mechanical model subsystem, described later.

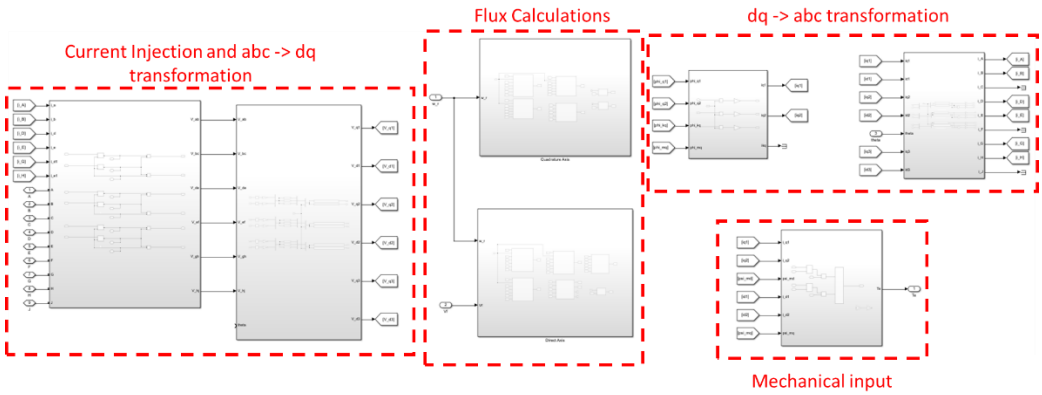

Figure 42. Subsystems within the electrical model of the nine-phase generator.

Initial current injection takes the feedback current from a previous time step and uses a Simulink current source block to generate the phase voltages in the a-b-c reference frame. Park's transformation equations are then used for transforming these phase voltages in the a-b-c reference frame into a d-q reference frame. Then, flux linkage calculations are performed using the Equations 3 – 7:

$$\frac{d\psi_{q,x}}{dt} = \omega_b \left[v_{q,x} - \left(\frac{\omega_r}{\omega_b}\right)\psi_{d,x} - \left(\frac{r_x}{X_x}\right)\left(\left(X_{lm} + \sum_{x\neq y,y=1}^{3} X_{l,y}\right)\psi_{q,x} - \sum_{x\neq y,y=1}^{3} X_{lm}\psi_{q,y} - \sum_{x\neq y,y=1}^{3} X_{l,y}\psi_{mq}\right) - X_{ldq}\left(\psi_{md} - \sum_{x\neq y,y=1}^{3} X_{d,y}\right)\right] \tag{3}$$

$$\frac{d\psi_{d,x}}{dt} = \omega_b \left[v_{d,x} - \left(\frac{\omega_r}{\omega_b}\right)\psi_{q,x} - \left(\frac{r_x}{X_x}\right)\left(\left(X_{lm} + \sum_{x\neq y,y=1}^{3} X_{l,y}\right)\psi_{d,x} - \sum_{x\neq y,y=1}^{3} X_{lm}\psi_{d,y} - \sum_{x\neq y,y=1}^{3} X_{l,y}\psi_{md}\right) - X_{ldq}\left(\psi_{md} - \sum_{x\neq y,y=1}^{3} X_{q,y}\right)\right] \tag{4}$$

$$\frac{d\psi_{fd}}{dt} = \omega_b \left[v_{fd} - \left(\frac{r_{fd}}{X_{fd}}\right)\left(\psi_{fd} - \psi_{md}\right)\right] \tag{5}$$

$$\frac{d\psi_{kq}}{dt} = \omega_b \left[v_{kq} - \left(\frac{r_{kq}}{X_{kq}} \right) (\psi_{kq} - \psi_{mq}) \right] \tag{6}$$

$$\frac{d\psi_{kd}}{dt} = \omega_b \left[v_{kd} - \left(\frac{r_{kd}}{X_{kd}} \right) (\psi_{fd} - \psi_{md}) \right] \tag{7}$$

The quadrature axis subsystem and a sample that demonstrates the above flux calculations is shown in Figure 43 (a) and (b), respectively. This methodology is replicated in the direct axis subsystem with the appropriate equations and parameters.

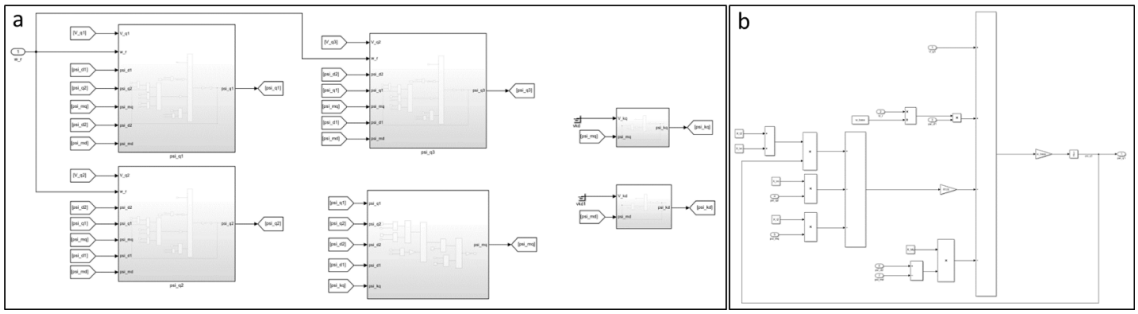

Figure 43. (a) Subsystem blocks for calculations in the quadrature axis where (b) individual flux linkage is computed for each of the three sets of phases.

The above equations to calculate the flux linkages are used to produce currents within the d-q reference frame which are then transformed back into the a-b-c reference frame using reverse Park's transformation equations. Then, these currents in the a-b-c reference frame at the current time step are fed back into the current injection subsystem for calculation of the system parameters for the subsequent time step. A separate subsystem was constructed to calculate the electrical torque using Equation (8):

$$T_e = \left(i_{q1} + i_{q2} + i_{q3}\right)\psi_{md} - (i_{d1} + i_{d2} + i_{d3})\psi_{mq} \tag{8}$$

This torque value is passed into the mechanical model, which is adapted from a well-established mechanical model developed by MATLAB/Simulink shown in Figure 44.

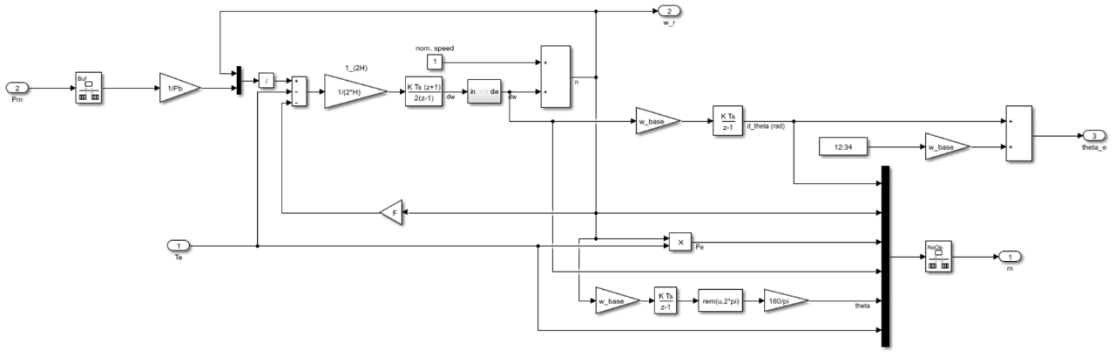

Figure 44. Mechanical subsystem used for computation of the speed variation within the generator.

The Simulink diagram, shown in Figure 44, models Equation (9) to calculate the speed variation within the generator:

$$\Delta\omega(t) = \frac{1}{2H}\int_0^t (T_m - T_e) - K_d\Delta\omega(t)dt \tag{9}$$

This speed is fed back into the electrical model and generator controller where the controller calculates an error between this value and a given reference to determine the amount of deviation that exists. It then acts to restore this value to its set point. The controller calculates the input that is fed back into the electrical model to create a closed-

loop system. Knowledge gained during the development of a motor-controller for the KATO three-phase generator was leveraged in this process and is shown in Figure 45. In this subsystem, the speed from the mechanical subsystem, Figure 44, is the input and this speed is compared to a reference value where a PI controller is used to restore the value to its set-point. Output from the PI controller becomes the mechanical torque of the machine and serves as the input into the induction motor, which is used as the input into the generator to control its rotational speed.

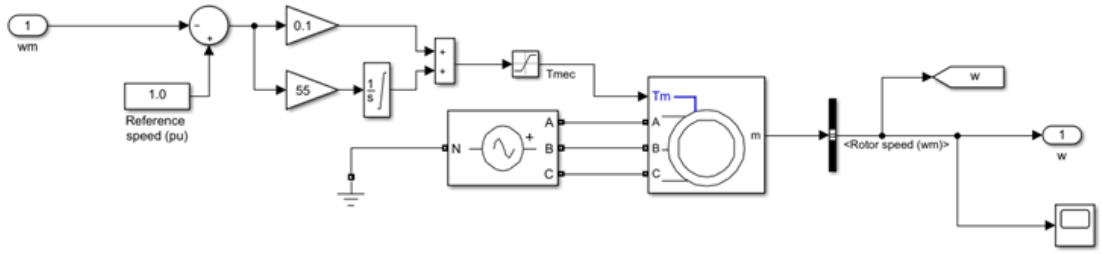

Figure 45. Induction motor model for motor-generator set.

The generator also requires an excitation system to control the field voltage of the machine. There is already a verified model within Simulink that implements an IEEE Type AC4A excitation system to calculate the field voltage based on feedback of the voltage in the d-q reference frame from the electrical model. This subsystem is shown in Figure 46 and was integrated in this modeling effort as the field voltage input into the generator model.

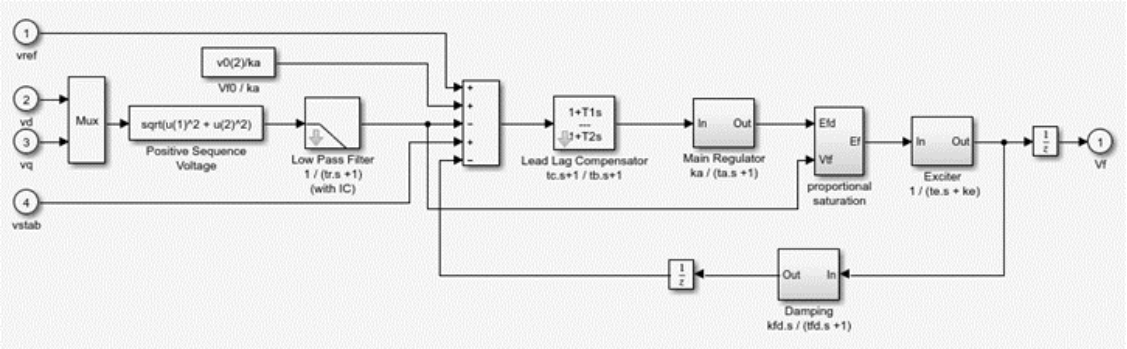

Figure 46. Simulink subsystem for IEEE Type AC4A exciter.

The nine-phase equivalent circuit and flux equations have several variables that must be provided as constants for calculation purposes. It is possible to numerically determine these values using finite element analysis (FEA) and modeling methods; however, this can be a time-consuming process and requires additional machine dimensions that were not available at the time. KATO was able to assist by deriving the required variables using in-house analytical calculations which derive the parameters faster than FEA methods but with reasonably comparable results. The general machine parameters are listed in Table 10 and more specific resistance and reactance values are listed in Table 11. These parameters were added into a MATLAB script that is referenced by the Simulink model before the model initiates, which provides ease of adjustment when fine-tuning these values after data has been collected.

Table 10. General machine parameters.

Parameter	Measurement
Voltage	683.3 V
Apparent Power	43.5 kVA
Power Factor	0.92
Phase Current	12.25 A
Frequency	120 Hz
Phases	9

Table 11. Machine reactance and resistance values.

Parameter	% p.u.	Ω	mH
X_d	65.59	21.12	28.01
X_q	36.25	11.67	15.48
X_l	13.41	4.32	5.73
X_{md}	52.18	16.80	22.29
X_{mq}	22.84	7.35	9.75
X'_{lfd}	4.28	1.38	1.83
X'_{lkd}	4.81	1.55	2.06
X'_{lkq}	0.36	0.11	0.15
R_s	3.98	1.28	---
R_{fd}	26.10	8.41	---
R'_{fd}	0.15	0.05	---
R'_{kd}	---	0	---
R'_{kq}	---	0	---

In addition to the parameters provided in Tables 11 and 12, KATO also provided the following information for modeling development purposes based on initial testing performed before the machine delivery date:

- Nameplate AC rating of the 9-phase generator is approximately 711 VAC L-L and 43.5 kVA and 40 kW
  - Current per phase should be about 12 A rms
  - Voltage per phase should be about 410.5 V rms
- The 0 - pk voltage per phase should be about 581 V and line-line 0 - pk voltage per phase should be about 1006 V
- The 0 - pk current per phase should be about 17 A
- The rated frequency range of the generator is 100 - 140 Hz

These values were verified in the model by connecting the output of the generator to an active power per phase of 13.33 kW constant power load, shown in Figure 47. The

resulting voltage and current were also recorded for each of the nine phases in the generator under these testing conditions.

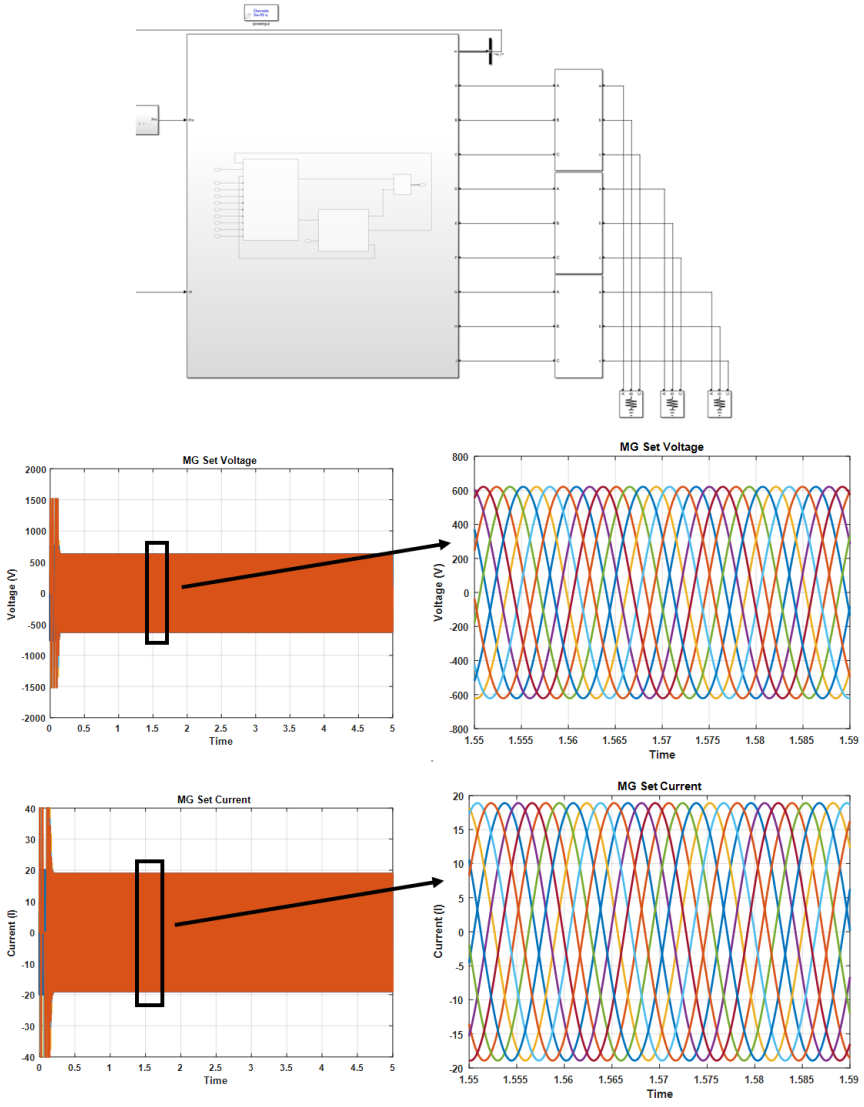

Figure 47. Machine model connected to a constant power load (top) and the resulting generator voltage (middle) and current (bottom) for each phase during this loading profile.

Based on Figure 47, it is observed that the model reaches steady state conditions within 0.25 sec under a constant power load condition. Each phase is separated by 40^{o} with

a frequency of ~120 Hz, the voltage per phase is about 600 V, the line-to-line voltage is about 1075 V, and the current per phase is about 17 A. These results match closely to the expected results provided by KATO engineers.

In addition to developing the motor-generator model, there is an 18-pulse active rectifier on the output of the generator that was also developed within Simulink. Development of this model leveraged previous work performed at UTA involving testing and modeling of different rectification systems. For this effort, a SCR based six-pulse rectifier was developed and connected to each of the three phases of the machine and then combined to create the full 18-pulse rectified DC output voltage. The model was developed with gating that can be adjusted to account for different firing angles based on the zero-point crossing of the AC waveform. The developed rectifier model and representative results are shown in Figure 48.

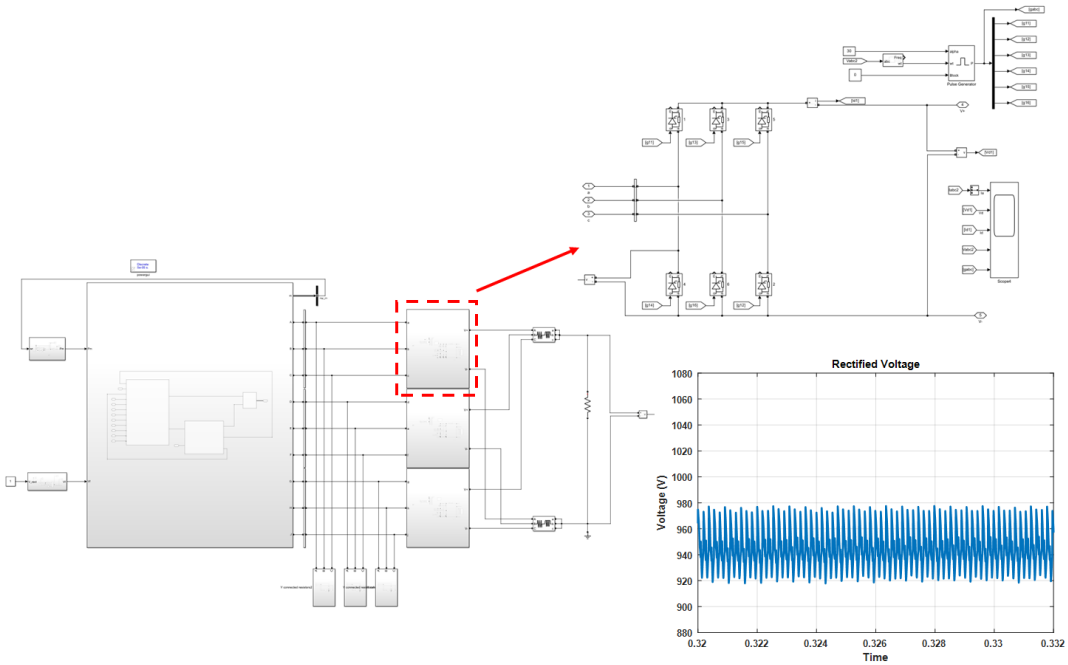

Figure 48. Model of the 18-pulse rectifier connected to the motor-generator set and representative results for the DC voltage.

A top-level view of the full motor-generator set and active rectifier model developed in Simulink is shown in Figure 49. Each aspect of the model is divided into its respective subsystem for aesthetic purposes as well as ease of development and troubleshooting, when needed.

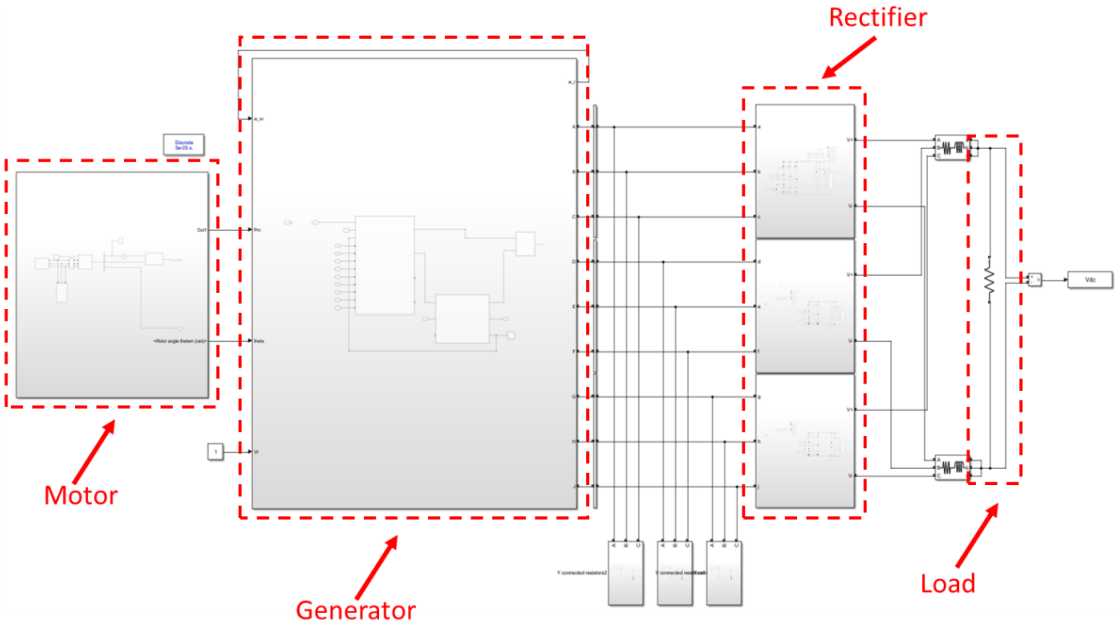

Figure 49. Top-level Simulink model of motor-generator set with 18-pulse rectifier and external resistive load.

4.2.2 Equipment Installation

The motor-generator set was installed into the UTA IDEAL, shown in Figure 50. As shown in Figure 4, the rectified output of the generator connects directly to the 1 kV bus where there is also 1 kV energy storage provided by a Saft VL30AFe lithium-ion battery. The SCR rectifier is controlled using a the BAP1950A SCR driver manufactured by

Applied Power Systems (APS). Currently that driver only works in an open loop control mode, but plans are in the works to close that loop to implement current control of the output.

After the machine was installed, additional monitoring was added to the generator to collect data for model verification and to observe current and voltage in real-time. Hall effect current sensors were added to each phase of the machine and one external voltage probe was added on one phase. Another voltage probe was added to the 1 kV DC bus. All current measurements and the two voltage measurements were measured and recorded in real-time using a custom LabVIEW VI. Some of the additional monitoring installed is shown in Figure 51 and the 1 kV DC external voltage probe is shown later in Figure 55.

Figure 50. Photographs showing the 40-kW machine after installation.

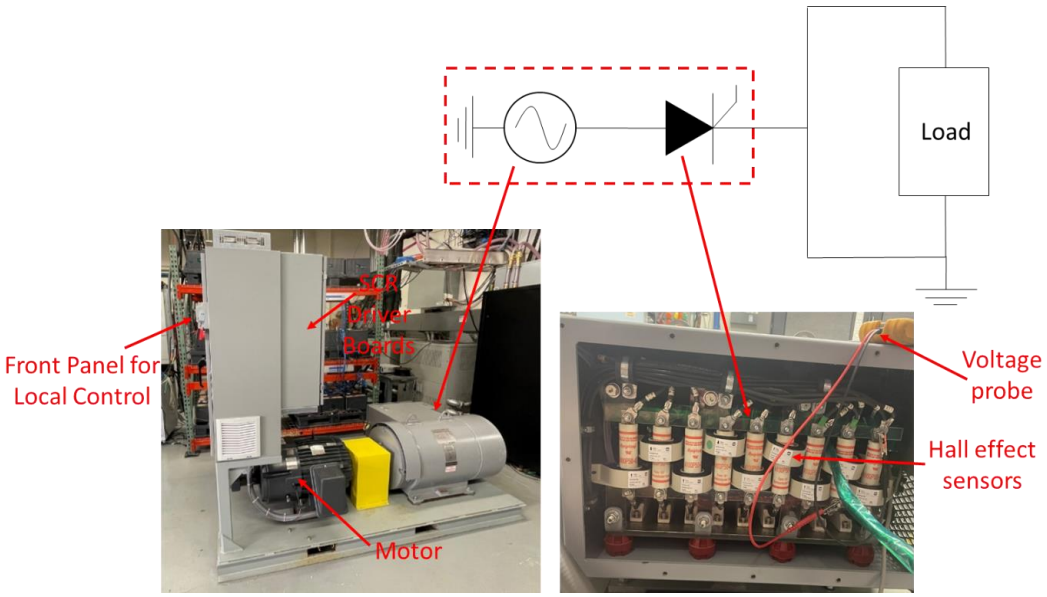

Figure 51. Schematic of the motor, generator, and rectifier. The machine was retrofitted with Hall effect sensors on each phase of the generator and an additional voltage probe was connected to one phase for monitoring of electrical parameters during operation.

Control of the motor-generator set is accomplished through the touchscreen on the front panel of the machine. After the breaker is flipped, the machine is initialized and the AC voltage is enabled followed by the DC voltage using the human interface device (HID). The AC voltage, frequency, and DC voltage can be adjusted by changing the set points on the front panel or using a 0 – 10 V analog input signal. The values of the frequency and voltages can be read in real-time from this front panel and any faults that occur while the machine is running can also be viewed from this panel. A view of the HID during normal operation, as well as faulted operation, is shown in Figure 52.

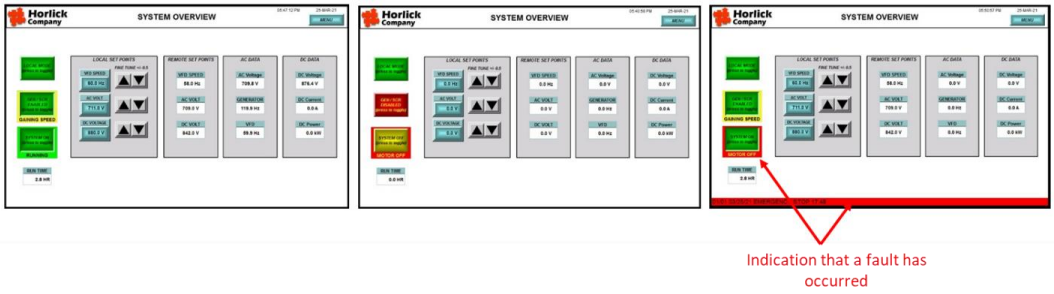

Figure 52. Normal (left) and faulted (middle and right) conditions as displayed on the HID located on the front of the machine.

A custom LabVIEW VI was written that provides a method to verify the values displayed on the front panel of the machine and save the data recorded by the current sensors placed on each of the nine phases, one AC voltage, and the DC voltage. Initial testing of the machine involved adjusting the set points on the front panel while the machine is loaded with a ceramic 120 Ω resistor. A view of the HID on the front of the machine compared with the LabVIEW VI computer display are shown in Figure 53 while the machine is loaded.

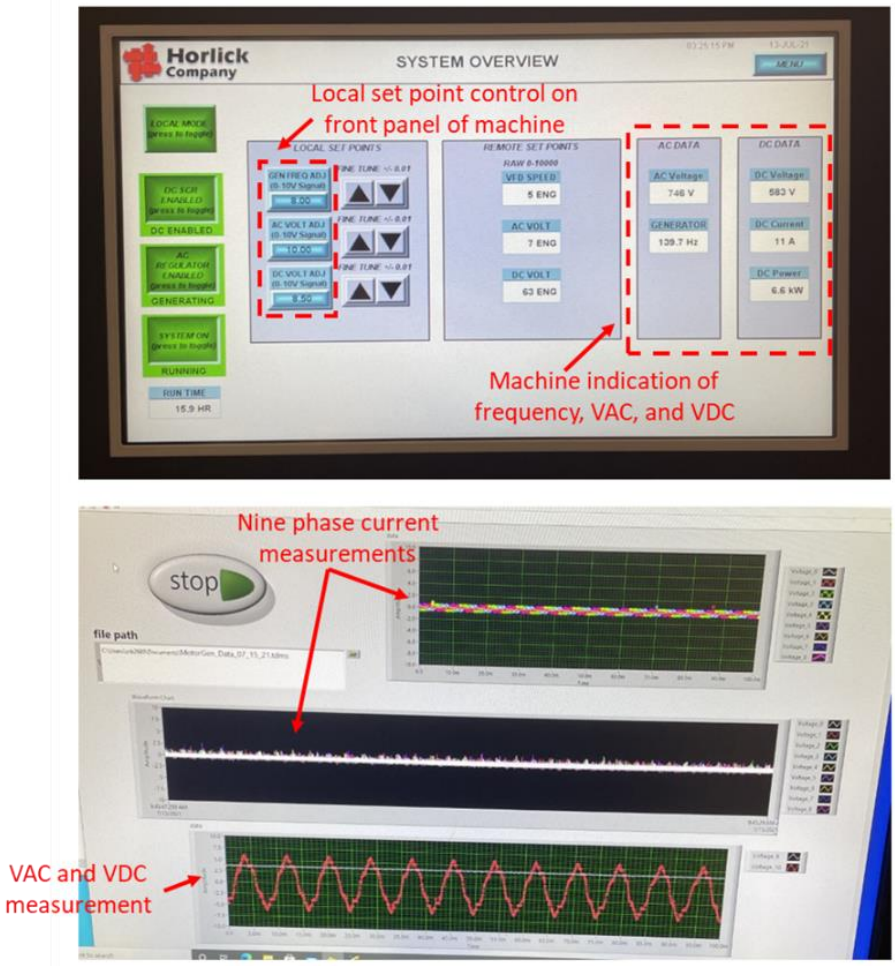

Figure 53. HID display when the machine's AC and DC are both enabled and the corresponding measurements observed in a custom LabVIEW VI.

While connected to a 120 Ω resistor, the AC voltage, the frequency of the generator, and the DC voltage were adjusted manually using the set-points on the front panel of the machine. The HID and the LabVIEW VI were used to observe how changing these set-points affects the machine's behavior. The LabVIEW software actively saves the nine-phase currents, one AC voltage, and the DC voltage at the 1 kV bus. Representative machine data was collected using the following frequency, VAC, and VDC set-points on the machine:

- Frequency = 8.00
- AC Voltage = 6.50
- DC Voltage = 10.00

Plots of the phase currents and DC voltage are shown below in Figure 54.

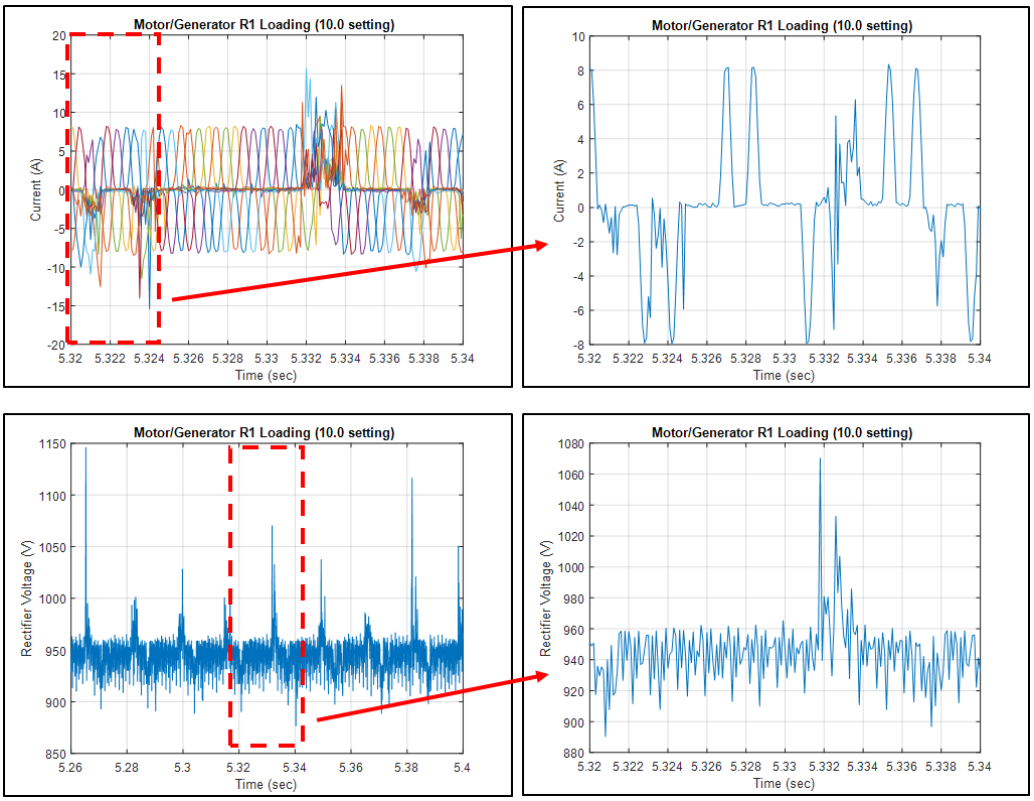

Figure 54. Representative results from current and voltage sensors located on the output of the machine and the 1 kV bus, respectively.

4.2.3 Model and Experimental Results

Figure 4 shows how the motor-generator set is integrated into the UTA IDEAL testbed. The 1 kV rectified DC output is directly connected to a bus where a combination of resistive and capacitive loads can be connected. Additionally, the testbed has a 1 kV

lithium-ion battery that can be added to the bus for buffering the generator during transient loading events. Initially, a resistive load bank was constructed using six high energy, high power, ceramic resistors connected in parallel. A mechanical, normally open, Ross relay, shown in Figure 55 was connected in series with each resistor to be able to drop the series resistance in subsequent tests. The total equivalent resistance of this network allows for testing that nearly reaches the limits of the machine's current capabilities and allows for step and transient loading at different resistive values. Only five of the six resistors were used during this testing effort to ensure that the generator did not exceed its maximum current rating. That data is shown in Figure 56.

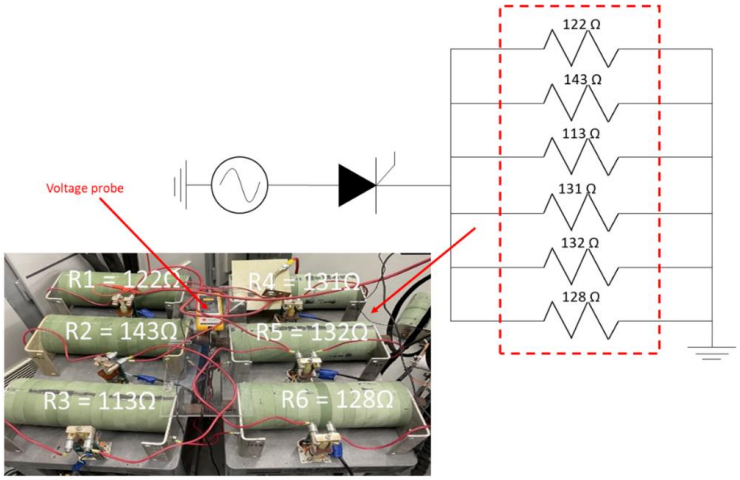

Figure 55. Resistive load bank consisting of six ceramic resistors connected in parallel and actuated using Ross relays. A voltage probe was also connected to the 1 kV bus for measurement and display of bus voltage in real-time within a custom LabVIEW VI.

In the first set of experiments performed, the generator was energized with the DC output voltage of roughly 930 V enabled. After running for at least 30 seconds, a single Ross relay was closed transiently loading the generator with roughly 120 Ω. This equates to a current draw of roughly 6.9 A, 5.7 kW. That plot is shown in the upper left hand corner

of Figure 56. Initially the voltage sags to around 870 V before recovering around 300 ms later to a steady state conduction voltage of 880 V. Next the DC voltage was disabled and then the Ross relay was returned to an open contact state. Trying to open the relay while the generator's DC output was energized resulted in an arc forming between the relay contacts that would persist due to the high current flowing. This process was repeated 4 more times, each time adding in an additional parallel resistor to the transient load. The four plots of those experiments are also shown in Figure 56. Notice that as the resistance decreases, and the transient load added to the generator increases, the voltage sag on the bus and the resulting recovery overshoot also increases. This is expected and is a direct reflection of the stiffness of the source. As will be shown later, this can be improved by buffering the generator with energy storage. In the final experiment shown in the lower right corner of Figure 56, a stairstep experiment was performed where the load was incrementally changed by adding one resistor every few hundred msec until all load is applied. This process was repeated multiple times with different rectifier voltage settings and the data was used to validate the Simulink model's transient representation.

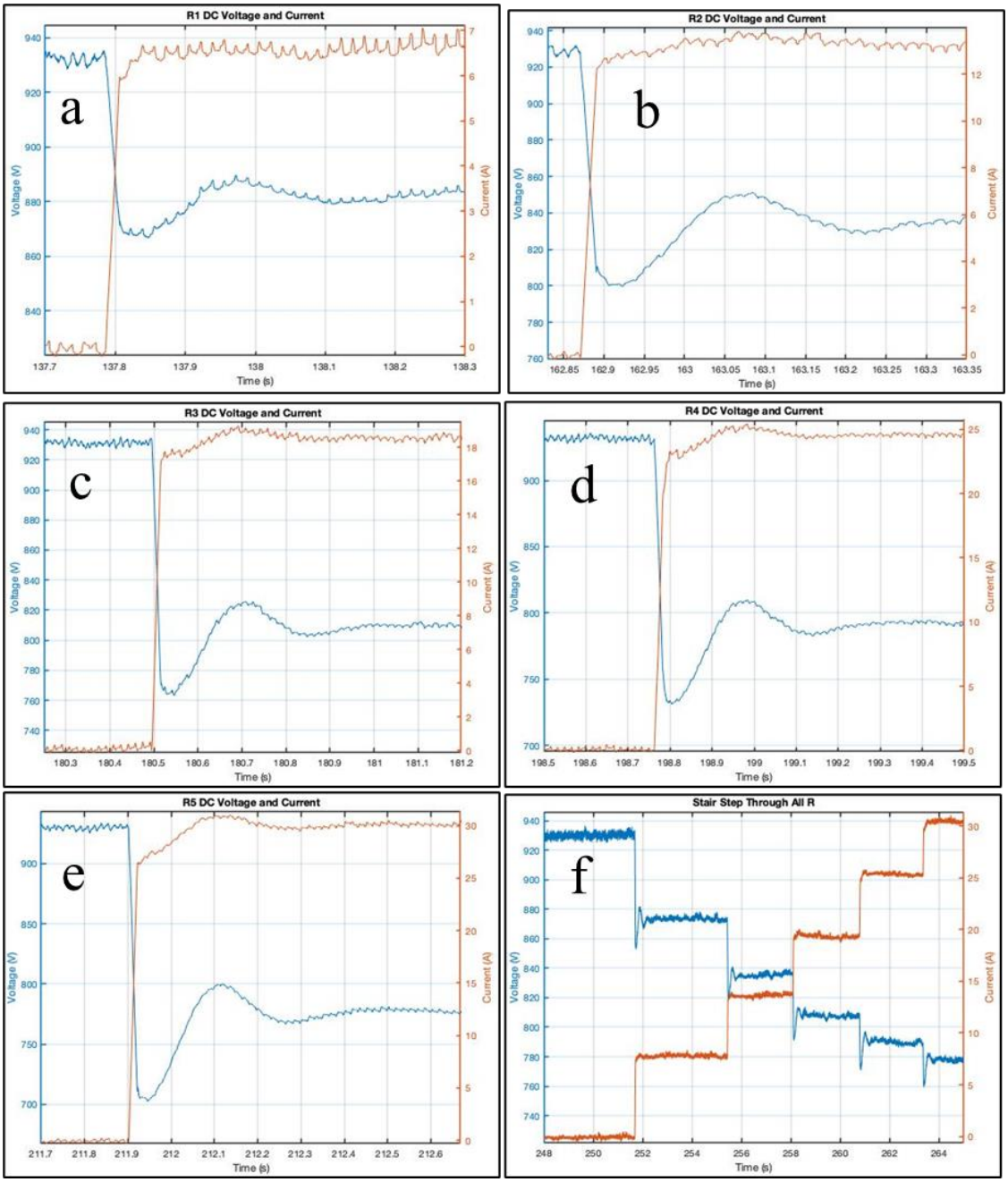

Figure 56. (a-e) Transient loading the generator with resistors 1 – 5 by adding each into the circuit in succession using Ross relays. (f) Transient loading of the generator with five loading steps between ~120 Ω and 20 Ω.

Steady state results captured from the generator's 9 phases during one experiment while a loaded with 120 Ω load is shown in the upper left corner of Figure 57. A comparison of one phase against the model results are shown in the upper right plot of Figure 57. Measured vs. modeled generator voltage and rectifier voltages are shown in the lower plots of Figure 57. Similar experiments are plotted in Figure 58 when the generator was loaded into a ~20 Ω resistive load. From these plots, it is observed that the Simulink model closely follows the voltage and current profiles of the actual hardware with exceptions expected due to switching effects that appear in models. Variation observed is expected from the switching behavior introduced in simulation tools.

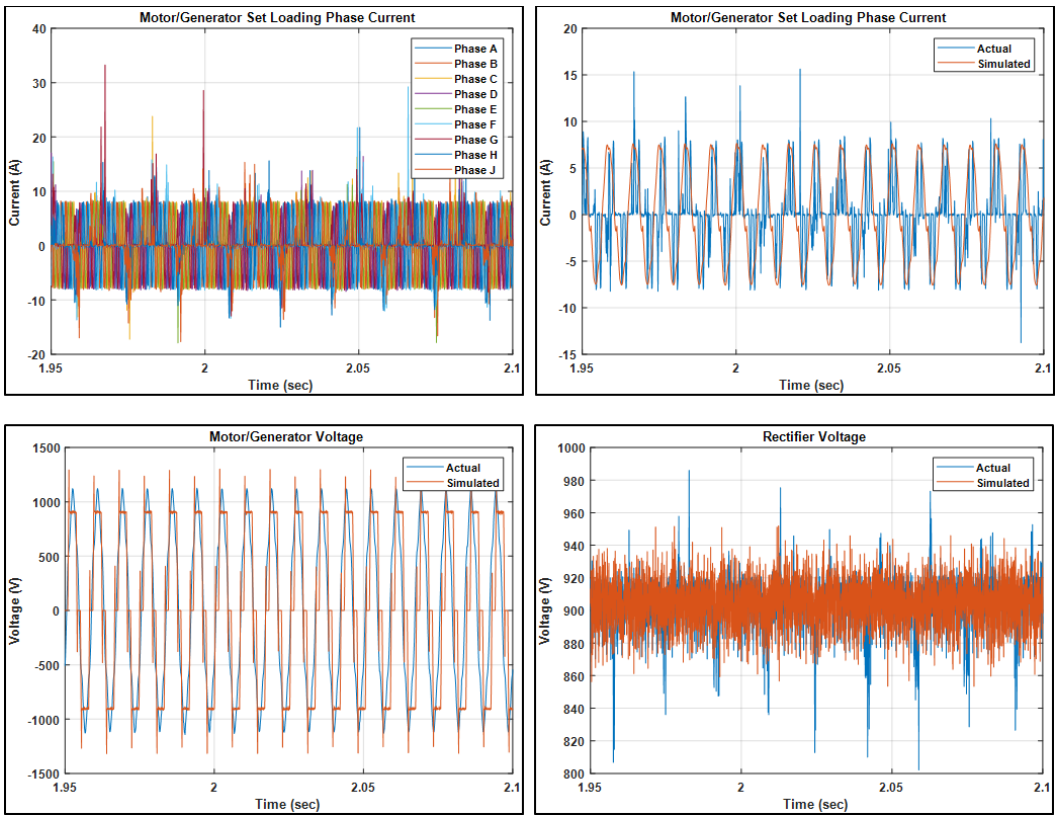

Figure 57. Experimental and modeling results from loading the generator with a 120 Ω resistive load.

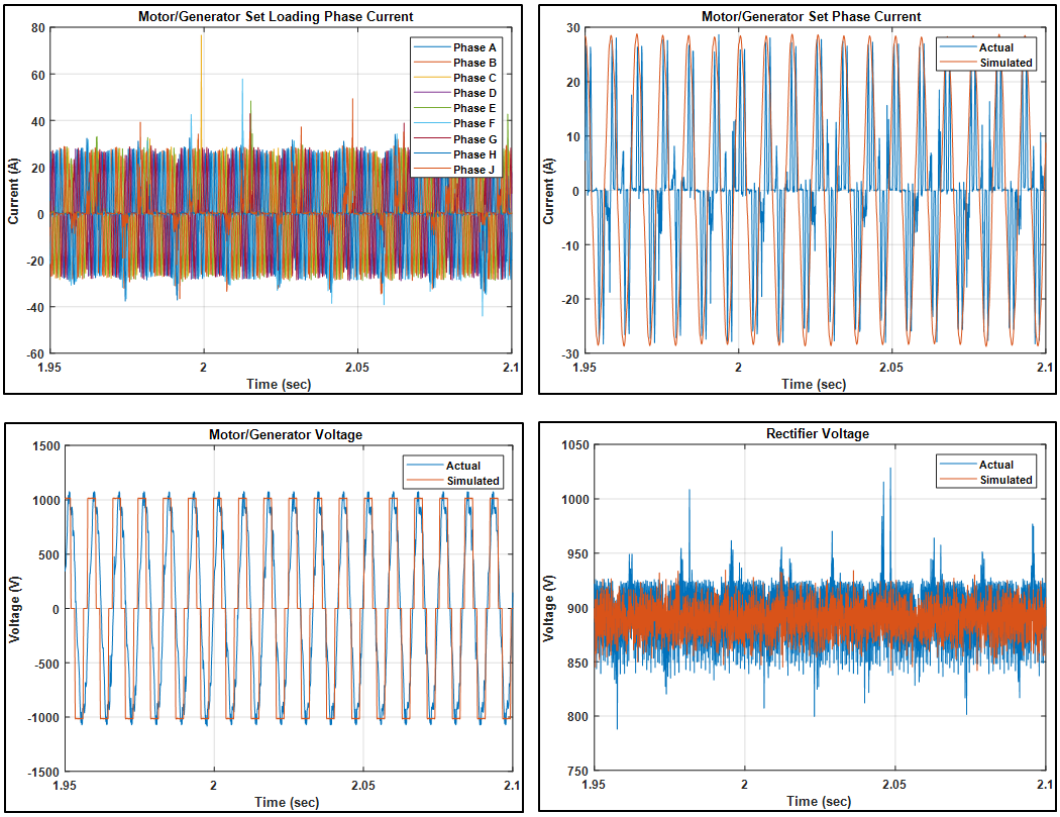

Figure 58. Experimental and modeling results from loading the generator with a ~20 Ω resistive load.

Next a series of experiments, seen in Figure 59, was performed to demonstrate the real time voltage regulation capability of the rectifier.

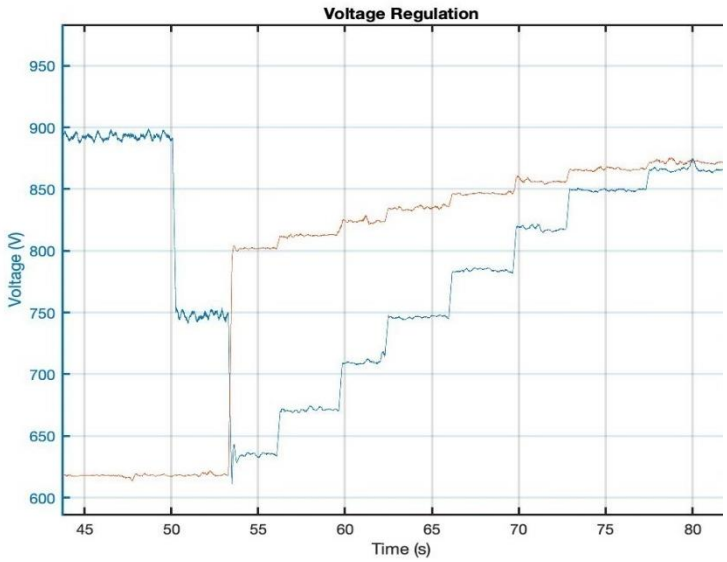

Figure 59. Experimental results demonstrating variability of the generator's DC output into a ~25 Ω resistive load.

At the start of the experiment, the rectifier is enabled with a 900 V setpoint and unloaded. At 50 seconds into the experiment, the rectifier setpoint was adjusted in an open load scenario to 750 V. At 53 second into the experiment, the rectifier was loaded with roughly 25 Ω. This causes the conduction voltage to sag to around 635 V conducting roughly 25 A. The voltage setpoint was then manually adjusted upwards periodically to demonstrate real-time control of the generator's setpoint. Since the rectifier run in open-loop control mode, an external controller is needed to actively regulate the voltage based off the load. That has not been done here simply due to time and resource constraints but its easily achievable. This plot demonstrates how a simple actively controlled rectifier can be used to dynamically set the DC output voltage.

Next a series of experiments were performed in which a 1000 V Saft VL30AFe battery was connected on the DC output bus, shown schematically in Figure 60. The battery

is made up of 260 VL30AFe cells connected in series. The data shown in Figure 61 demonstrates the ability to adjust the current supplied by the generator to recharge the battery.

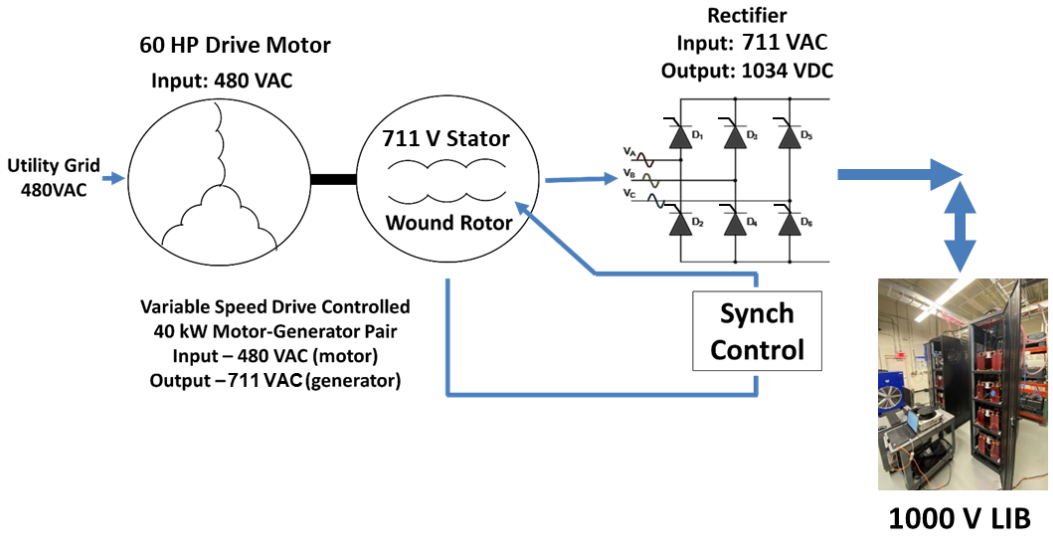

Figure 60. Experimental setup connecting a 1000 V battery to the generator output bus.

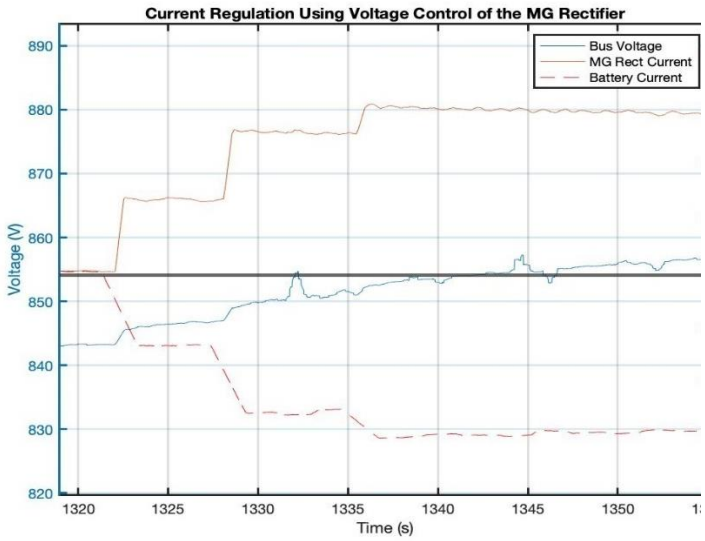

Figure 61. Experiment demonstrating the ability to dynamically adjust the battery recharge current supplied by the generator through rectifier rectification.

Next, an HV DC load was connected onto the bus as shown in Figure 62. In the first experiment shown in Figure 63, the DC bus is loaded with a constant current draw of 30 A. The dynamic of current share between the two sources is dependent upon each one's respective stiffness and impedance. Because the battery is the stiffer source, it dictates the bus voltage. The rectifier voltage was initially regulated to be very close to that of the battery. When the transient load comes on, the battery voltage sags just below the setpoint of the generator. The battery supplies 27 A of the 30 A load and the rectifier supplies the other 3 A.

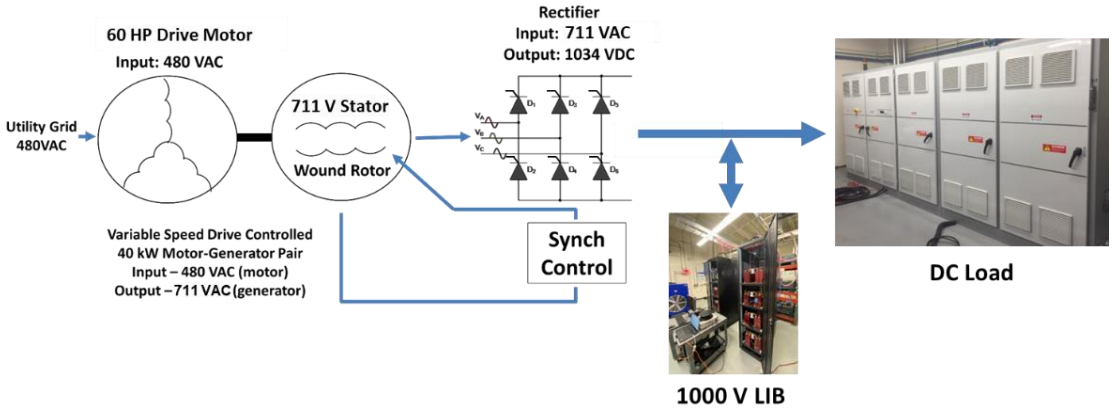

Figure 62. Experimental design for transient loading of the generator using a battery and the Chroma 17030.

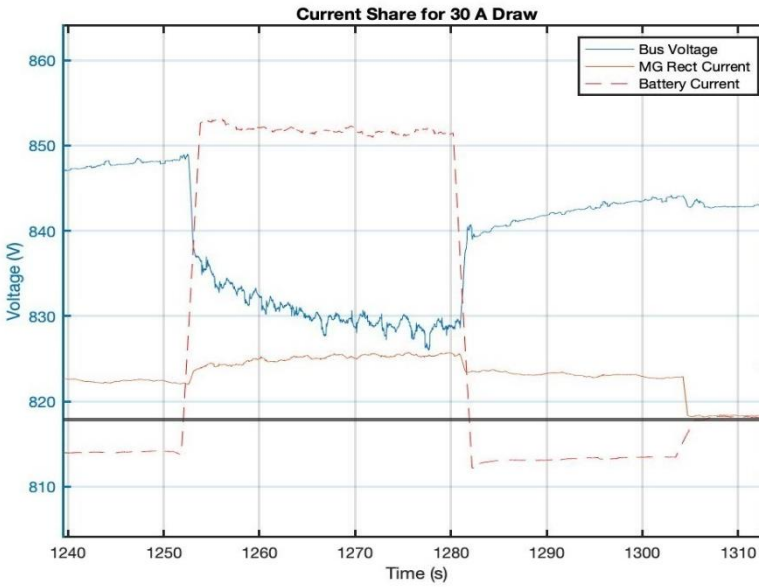

Figure 63. Experiment demonstrating current sharing between the motor-generator/rectifier set and the battery into a 30 A constant current load.

In the last experiment, shown in Figure 64, a 15 A constant current is pulled by the high voltage load. At the start of the experiment, the battery supplies nearly all the 15 A load. At 1195 s, the voltage of the rectifier was adjusted to slightly increase the current it supplies. Though it is a simple adjustment, it demonstrates the ability to dynamically control the power sharing between the battery and the generator as requested by the overarching controller.

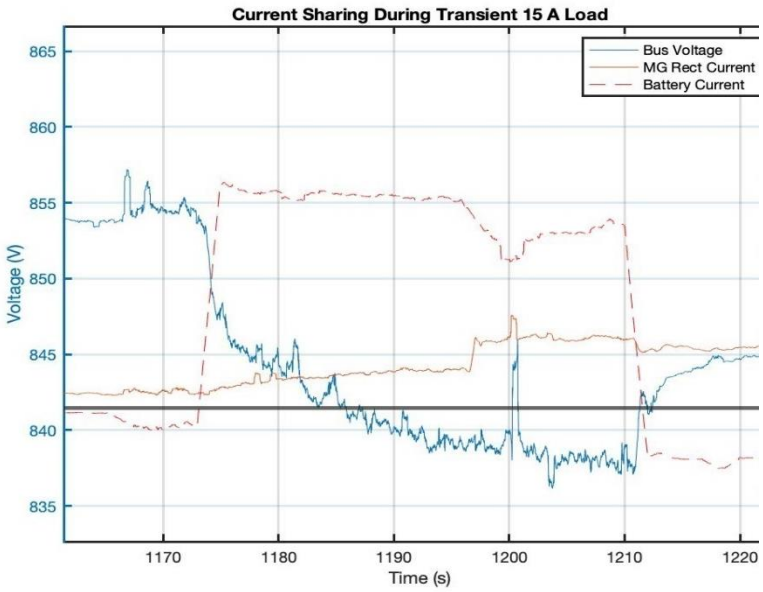

Figure 64. Experiment demonstrating actively adjusted current sharing between the motor-generator/rectifier set and the battery into a 30 A constant current load.

CONCLUSION

Future microgrid and naval applications will employ a combination of MVAC and MVDC architectures. These emerging structures will require a variety of equipment and components some of which have not been designed or developed yet. Particular interest will be given to energy storage and rotating machines since these are sources of DC and AC power, respectively, with advancements in power electronics creating an opportunity for traditional AC generators to be rectified to DC for applications in electrification. While it is possible to build and procure each of these electrical components, advancements in computational modeling have created opportunities for emulation of hardware through development of models that simulate the hardware's behavior under specified conditions. Eventual use of the models requires that verification and validation efforts be performed to ensure that the models generate results within a specified level of accuracy for their intended purpose. This process has been shown here for one battery chemistry and two M-G sets within the UTA IDEAL testbed. This modeling methodology can be used for further development of component models within the current testbed design or applied to other components that can then be placed in a simulation format. This provides a method for developing safer and more advanced microgrid structures without the need for acquiring each component as new items become available.

REFERENCES

1. J.F. Hansen and F. Wendt, 'History and State of the Art in Commercial Electric Ship Propulsion, Integrated Power Systems, and Future Trends,' Proceedings of the IEEE | Vol. 103, No. 12, December 2015.

2. G. Ortiz, J. Biela, D. Bortis, J.W. Kolar, "1 Megawatt, 20 kHz, Isolated, Bidirectional 12 kV to 1.2 kV DC-DC Converter for Renewable Energy Applications," *The 2010 International Power Electronics Conference – ECCE ASIA*, IEEE, 2010.

3. ONR Electric Ship Research Development Consortium, https://www.esrdc.com/, Online August 19, 2021.

4. U. Javaid, D. Dujic, W.V.D. Merwe, "MVDC Marine Electrical Distribution: Are we ready?," *IECON 2015 – 41st Annual Conference of the IEEE Industrial Electronics Society,* IEEE, 2015.

5. Office of Naval Research. "Hybrid Energy Storage Module (HESM): Amendment 001" 13-SN-0007 [Online]. Available: http://www.onr.navy.mil/~/media/Files/Funding-Announcements/Special-Notice/2013/13-SN-0007-Amendment-0001.ashx.

6. R.E. Hebner, K. Davey, J. Herbst, D. Hall, J. Hayne, D. Surls, A. Ouroua, "Dynamic Load and Storage Integration," *Proceedings of the IEEE,* IEEE, 2015.

7. S.G. Jayasinghe, L. Meegahapola, N. Fernando, Z. Jin, J.M. Guerrero, “Review of Ship Microgrids: System Architectures, Storage Technologies and Power Quality Aspects,” Inventions, MDPI, 2017.

8. N. Doerry and J. Amy, ‘MVDC Shipboard Power System Considerations for Electromagnetic Railguns,’ 6th DOD Electromagnetic Railgun Workshop, Laurel, MD, September 2017.

9. N. Doerry, H. Fireman, ‘Designing All Electric Ships,’ Proceedings of the Ninth International Marine Design Conference, 2006.

10. N. Doerry, ‘Zonal Ship Design,’ Naval Engineers Journal, 2008.

11. Electric Power Components and Systems, https://www.onr.navy.mil/en/Science-Technology/Departments/Code-33/All-Programs/331-advanced-naval-platforms/electric-power-components-and-systems, Office of Naval Research (ONR), 2021.

12. D. Paul, “A History of Electric Ship Propulsion Systems,” IEEE Industry Applications Magazine, IEEE, 2020.

13. IEEE, “Recommended Practice for 1 kV to 35 kV Medium-Voltage DC Power Systems on Ships,” IEEE Std. 1709-2010, IEEE, 2010.

14. G.F. Reed, B.M. Grainger, A.R. Sparacino, R.J. Kerestes, M.J. Korytowski, “Advancements in Medium Voltage DC Architecture Development with Applications for Powering Electric Vehicle Charging Stations,” 2012 IEEE Energytech, IEEE, 2012.

15. Johnston, A., Wetz, D., Madani, R., Davoudi, A., Turner, G., Dodson, D., McRee, B., Pullaguram, D., Bailey, Z., Heinzel, J., Giuliano, M., Schegan, C. “Mitigating Transient Loads in Medium-Voltage Direct Current Microgrids,” Advanced Machinery Technology Symposium, *American Society of Naval Engineers*, 2021.

16. Johnston, A.N., Wetz, D.A., Turner, G.K., Bailey, Z.R., Dodson, D.A., McRee, B.J., Heinzel, J.M. “A Medium Voltage AC and DC Distributed Power Generation Testbed Deploying Transient Loads,” *Proceedings* of the International Ship Control Systems Symposium, 2020.

17. Schlesinger, S., “Terminology for Model Credibility,” *Simulation*, Vol. 32, No. 3, 1979.

18. *IEEE-STD-610*, “A Compilation of IEEE Standard Computer Glossaries”, *IEEE Standard Computer Dictionary*, 1991.

19. Sargent, R.G. “An Introductory Tutorial on Verification and Validation of Simulation Models,” Proceedings of the 2015 Winter Simulation Conference, *IEEE*, 2015.

20. Sargent, R.G. “Verification and validation of simulation models,” *Journal of Simulation*, 2013.

21. Sargent, R.G. “Verifications and Validation of Simulation Models,” Proceedings of the 2010 Winter Simulation Conference, IEEE, 2010.

22. U.S. Department of Transportation, Systems Engineering for Intelligent Transportation Systems. https://ops.fhwa.dot.gov/publications/seitsguide/seguide.pdf, 2007.

23. Shionuma, K., Yokokawa, M, Nagaura, T. “Characteristics of lithium ion rechargeable battery.” *Abstracts 32nd Battery Symposium* 1991, 33-34.

24. Bretscher, E. “Lithium Battery Banks – Fundamentals.” https://nordkyndesign.com/lithium-battery-banks-fundamentals/, 2022.

25. Horiba, T. “Lithium-Ion Battery Systems.” *Proceedings of the IEEE* 2014.

26. Pender, J.P., Jha, G., Youn, D.H., Ziegler, J.M., Andoni, I., Choi, E.J., Heller, A., Dunn, B.S., Weiss, P.S. Penner, R.M., Mullins, C.B. “Electrode Degradation in Lithium-Ion Batteries.” *ACS Nano* 2020, 14(2), 1243-1295.

27. Colbow, KM., Dahn, JR., Haering, RR., “Structure and electrochemistry of the spinel oxides $LiTi_2O_4$ and $LiTi_{4/3}Ti_{5/3}O_4$,” *Journal of Power Sources* 1989, 397-402.

28. Purwanto, A., Muzayanha, S.U., Yudha, C.S., Widiyandari, H., Jumari, A., Dyartanti, E.R., Nizam, M., Putra, M.I. “High Performance of Salt-Modified-LTO Anode in $LiFePO_4$ Battery.” *Applied Sciences* 2020, 10, 7135.

29. Li, Y., Fu, G., Watson, M., Harrison, S., Paranthaman, M.P. “Monodispersed $Li_4Ti_5O_{12}$ with Controlled Morphology as High Power Lithium Ion Battery Anodes.” *ChemNanoMat* 2016, 2, 642-646.

30. Nagamine, M., Kato, H., Nishi, Y. “Characteristics of new lithium ion rechargeable batteries.” *Abstracts 33rd Battery Symposium* 1992, 83-84.

31. Scharner, S., Weppner, W., Schmid-Beurmann, P. “Evidence of two-phase formation upon lithium insertion into the $Li_{1.33}Ti_{1.67}O_4$ spinel.” *Journal of Elecrochemical Society* 1999, 857-861.

32. Han, X., Ouyang, M., Lu, L., Li, J. “Cycle Life of Commercial Lithium-Ion Batteries with Lithium Titanium Oxide Anodes in Electric Vehicles.” *Energies* 2014, 7(8), 4895-4909.

33. Takami, N., et al. “High-power and long-life lithium-ion batteries using lithium titanium oxide anode for automotive and stationary applications.” *Journal of Power Sources* 2013, 469-475.

34. Pine Research, EIS Basic Background. https://pineresearch.com/shop/kb/theory/eis-theory/basic-background-theory/, 2022.

35. Metrohm Autolab, Autolab PGSTAT302N, https://www.metrohm-autolab.com/Products/Echem/NSeriesFolder/PGSTAT302N, 2022.

36. Hou, J., Sun J., Hofmann, H.F. “Mitigating Power Fluctuations in Electric Ship Propulsion With Hybrid Energy Storage System: Design and Analysis,” *IEEE Journal of Oceanic Engineering*, 2018.

37. Wetz, D., Novak, P.M., Shrestha, B. “Development of a Power Electronic Test Stand for the Elevated Rate Recharge of Electrochemical Energy Storage Devices.” *2012 Twenty-Seventh Annual IEEE Applied Power Electronics Conference and Exposition (APEC)* 2012, 2159-2166.

38. Madani, S.S., Schaltz, E. Kaer, S.K. “An Electrical Equivalent Circuit Model of a Lithium Titanate Oxide Battery.” *Batteries* 2019, 5(1), 31.

39. Chin, M., Rincon-Mora, G.A. “Accurate electrical battery model capable of predicting runtime and I-V performance.” *IEEE Transactions on Energy Conversion* 2006, 21, 504-511.

40. Andre, D., Meiler, M., Steiner, K., Wimmer, Ch., Soczka-Guth, T., Sauer, D.U. “Characterization of high-power lithium-ion batteries by electrochemical impedance spectroscopy. I. Experimental investigation.” *Journal of Power Sources* 2011, 196, 5334-5341.

41. Thanagasundram, S., Arunachala, R., Makinejad K., Teutsch, T., Jossen, A. “A Cell Level Model for Battery Simulation.” *European Electric Vehicle Congress* 2012.

42. Takei, K., Kumai, K., Kobayashi, Y., Miyashiro, H., Terada, N., Iwahori, T., Tanaka, T. “Cycle life estimation of lithium secondary battery by extrapolation method and accelerated aging test.” *Journal of Power Sources* 2001, 97-98, 697-701.

43. MIL-STD-1399 (Section 300B), “Electric Power, Alternating Current,” *Department of Defense Interface Standard*, 2008.

44. G.K. Singh, “Modeling and analysis of six-phase synchronous generator for stand-alone renewable energy generation,” *Energy* 36 (2011) 5621-5631.

45. Dehkordi, A.B. “Development of a Symmetrical Multi-Phase Synchronous Machine Model for Real-Time Digital Simulation,” *International Conference on Power Systems Transients,* 2017.

46. Kulkarni, S.S., Thosar, A.G. “Mathematical Modeling and Simulation of Permanent Magnet Synchronous Machine,” *International Journal of Electronics and Electrical Engineering,* 2013.

47. Aliprantis, D.C., Sudhoff, S.D., Kuhn, B.T. “A Synchronous Machine Model With Saturation and Arbitrary Rotor Network Represenation,” *IEEE Transactions on Energy Conversion,* 2005.

48. Kuzle, I., Krpan, M. “Detailed mathematical and simulation model of a synchronous generator,” *Journal of Energy,* 2015.

49. Toirov, O., Bekishev, A., Urakov, S., Mirkhonov, U. “Development of Differential Equations and their Solution Using the Simulink Matlab Program, which Calculate the Self-Swinging of Synchronous Machines with Traditional and Longitudinal-Transverse Excitation,” *E3S Web of Conferences,* 2020.

50. Singh, G.K., Iqbal, A. “Modeling and Analysis of Six-Phase Synchronous Motor under Fault Condition,” *Chinese Journal of Electrical Engineering,* 2017.

51. Singh, M., Gupta, S., Yadav, K.B., “Multiphase Induction Generator (Modeling, Analysis and Simulation) and Power Quality,” *International Journal of Scientific & Engineering Research,* 2013.

52. Rockhill, A.A., Lipo, T.A. “A Simplified Model of a Nine Phase Synchronous Machine Using Vector Space Decomposition,” *Electric Power Components and Systems,* 2009.

53. Venna, S.G.R., Vattikonda, S., Mandarapu, S. “Mathematical Modeling and Simulation of Permanent Magnet Synchronous Motor,” *International Journal of Advanced Research in Electrical, Electronics, and Instrumentation Engineering*, 2013.

54. Iqbal, A., Singh, G.K., Pant, V. “Steady-state modeling and analysis of six-phase synchronous motor,” *Systems Science & Control Engineering: An Open Access Journal,* 2014.

55. Dejia, Z., Zhengning, Z., Shanming, W., Jianyun, C. “Vector Control for a Twelve-Phase Synchronous Motor,” *Proceeding of International Conference on Electrical Machines and Systems,* 2007.

56. Singh, G.K. “Multi-phase induction machine drive research – a survey,” *Electric Power Systems Research,* 2002.

57. Jaganathan, S., Palaniswami, S., Adithya, R. “Synchronous Generator Modeling and Analysis for a Microgrid in Autonomous and Grid Connected Mode,” *International Journal of Computer Applications,* 2011.

58. Krause, P., Wasynczuk, O., Pekarek, S. *Electromechanical Motion Devices, Second Edition*. 2012.

59. Rathika, N., Kumar, S., Rahul, S. “Assessment of Six Phase Synchronous Generator Using Fuzzy Controller,” Lecture Notes in Electrical Engineering, 2015.

60. Shahnazari, M., Vahedi, A. “Average Value Modeling of Synchronous Machine-Rectifier System Considering Stator Resistance,” *IEEE,* 2009.

61. Jaskevich, J., Pekarek, S.D., Davoudi, A. “Parametric Average-Value Model of Synchronous Machine-Rectifier Systems,” *IEEE Transactions on Energy Conversion,* 2006.

62. Demiroren, A., Zeynelgil, H.L., “Modeling and simulation of synchronous machine transient analysis using SIMULINK,” *International Journal of Electrical Engineering Education,* 2002.

63. Kalaivani, C., Rajambal, K. “Dynamic Modeling of Seven-Phase Induction Generator,” *1st International Conference on Power, Computing and Control*, 2017.